

Supervised learning for robust quantum control in composite-pulse systems

Zhi-Cheng Shi^{1,2}, Jun-Tong Ding^{1,2}, Ye-Hong Chen^{1,2,3,4,*}, Jie Song⁵, Yan Xia^{1,2,†}, X.X. Yi^{6,‡} and Franco Nori^{3,4,7}

¹*Fujian Key Laboratory of Quantum Information and Quantum Optics, Fuzhou University, Fuzhou 350108, China*

²*Department of Physics, Fuzhou University, Fuzhou 350108, China*

³*Theoretical Quantum Physics Laboratory, Cluster for Pioneering Research, RIKEN, Wakoshi, Saitama 351-0198, Japan*

⁴*Quantum Information Physics Theory Research Team, Center for Quantum Computing, RIKEN, Wakoshi, Saitama 351-0198, Japan*

⁵*Department of Physics, Harbin Institute of Technology, Harbin 150001, China*

⁶*Center for Quantum Sciences and School of Physics, Northeast Normal University, Changchun 130024, China*

⁷*Department of Physics, University of Michigan, Ann Arbor, Michigan 48109-1040, USA*



(Received 22 August 2023; revised 31 January 2024; accepted 14 March 2024; published 4 April 2024)

In this work, we develop a supervised learning model for implementing robust quantum control in composite-pulse systems, where the training parameters can be either phases, detunings, or Rabi frequencies. This model exhibits great resistance to all kinds of systematic errors, including single, multiple, and time-varying errors. We propose a modified gradient descent algorithm for adapting the training of phase parameters, and show that different sampling methods result in different robust performances. In particular, there is a trade-off between high fidelity and robustness for a given number of training parameters, and both can be simultaneously enhanced by increasing the number of training parameters (pulses). For its applications, we demonstrate that the current model can be used for achieving high-fidelity arbitrary superposition states and universal quantum gates in a robust manner. This work provides a highly efficient learning model for fault-tolerant quantum computation by training various physical parameters.

DOI: [10.1103/PhysRevApplied.21.044012](https://doi.org/10.1103/PhysRevApplied.21.044012)

I. INTRODUCTION

Quantum control with high precision is an essential prerequisite for the implementation of reliable quantum computation [1]. Here, high precision has two meanings: one for perfect control, with knowledge of given physical parameters, and the other for being as free as possible from the effects of various systematic errors. The former is readily attainable, for instance, by adopting the familiar resonant pulse technique [2]. The latter is truly difficult and requires a great deal of attention. One of the main reasons is that we cannot really capture the complicated nature of systematic errors, such as the inevitable perturbations in parameters and decoherence noises. Thus far, numerous approaches have been put forward to address them, including adiabatic passage [3–6],

dynamical decoupling [7–9], quantum feedback [10–13], single-shot-shaped pulses [14,15], derivative removal by an adiabatic gate [16–18], sampling-based algorithms [19–21], geometric optimization [22–26], and robust optimal control [27–31].

The emergence of machine learning [32] offers another powerful way to tackle the issue of robustness against various errors. Essentially, machine learning is a process of using data to learn the rules applicable to it, and then utilizing the learned rules to make predictions on new data. Typical algorithms involved in machine learning are decision trees, neural networks, support vector machines, random forests, and collaborative filtering, to name a few [33]. Broadly speaking, machine learning can be divided into three main categories: unsupervised learning, supervised learning, and reinforcement learning. Over the last few years, machine learning, especially supervised learning, has achieved great success in many fields of physics [34–38], such as the study of nonequilibrium quantum dynamics problems [39–47], the classification of quantum states [48–53], and the design of control fields for high-fidelity quantum gates [54–62].

*Corresponding authors: cyhong_jmu@163.com

†xia-208@163.com

‡yixx@nenu.edu.cn

To date, a variety of methods, e.g., the Krotov [63], gradient ascent pulse engineering (GRAPE) [64], evolutionary [65–67], and variational quantum algorithms [68], have been raised to update variables in optimization problems. Among them, the high-efficiency GRAPE algorithm [64] and its variants [69–74] are successful in designing the control fields to sharply suppress the influence of various errors, e.g., amplitude uncertainty and frequency drift. Recently, there has been an increasing interest in the combination of GRAPE with other methods, such as the chopped random basis [75–77], generally referred to as gradient optimization using the parametrization algorithm [78]. In particular, de Fouquieres *et al.* [79] showed that the gradient accuracy and the convergence rate of the GRAPE algorithm can be effectively improved by introducing the Broyden-Fletcher-Goldfarb-Shanno quasi-Newton algorithm [80].

In this work, we provide a systematic methodology for robust quantum control through constructing a supervised learning model in composite-pulse systems. This model is quite universal and very robust to all kinds of systematic errors, including single error, multiple types of errors, time-varying errors, and so forth. Specifically, we establish the cost function of the supervised learning model, and then propose a modified version of the GRAPE algorithm to update the phases. The learned parameters (e.g., phases or detunings) possessing robustness against all kinds of systematic errors are subsequently determined via training the sample set.

In the current model, one of the most critical steps is to ascertain the *sampling* method, which allows us to obtain the sampling distributions. We demonstrate that it is necessary to select a suitable sampling distribution to receive robust and high-fidelity quantum control. Furthermore, the generalization ability of this model is significantly enhanced by increasing the number of pulses. We finally extend this model to train any physical parameters to implement robust quantum control. Our method paves an efficient way toward the establishment of reliable quantum gates for fault-tolerant quantum computation.

The rest of this paper is organized as follows. In Sec. II, we introduce the physical system and the possible difficulties in composite pulses. In Sec. III, we first show how to design the cost function for the supervised learning model. Next, we propose a modified gradient descent algorithm to train the phase parameters, and then investigate in detail the sampling method and the generalization ability of this model. In Sec. IV, we provide some applications for this model, including the implementation of arbitrary superposition states and general single-qubit gates, which are robust against all kinds of systematic errors. In Sec. V, we show that this model has the ability to train any physical parameters to achieve robust quantum control in different quantum systems. Conclusions are given in Sec. VI.

II. PHYSICAL MODEL

Consider a qubit coherently driven by a control field; the general form of the Hamiltonian in the interaction picture reads ($\hbar = 1$)

$$H(\theta) = \Delta\sigma_z + \Omega e^{-i\theta}\sigma_+ + \Omega e^{i\theta}\sigma_-, \quad (1)$$

where Δ represents the detuning between the transition frequency of the qubit and the carrier frequency of the control field, Ω is the Rabi frequency, θ denotes the phase, and $\sigma_{\pm} = \frac{1}{2}(\sigma_x \pm i\sigma_y)$, with σ_v ($v = x, y, z$) being Pauli operators.

To achieve general single-qubit gates, the most intuitive and fastest method is to exploit a resonant pulse, i.e., $\Delta = 0$. Then, the evolution operator of this system becomes (up to a global phase)

$$\mathcal{U}(\theta) = e^{-iH(\theta)t} = \begin{bmatrix} \cos A & -ie^{i\theta} \sin A \\ -ie^{-i\theta} \sin A & \cos A \end{bmatrix} \quad (2)$$

with pulse area $A = \Omega t$. In the ideal case, one can effortlessly obtain a multitude of perfect single-qubit gates by simply choosing different pulse areas and phases. Considering the imperfect knowledge of quantum systems, there are two typical types of systematic errors: pulse area errors and off-resonance effects.

Pulse area errors usually originate from incorrect duration and deviation in the Rabi frequency. The former is mainly caused by the inability of selecting a precise operation time. For instance, when an atomic beam passes through a laser field, the interaction times between the atoms and the laser field may be different because of the distinct longitudinal velocities of atoms [81]. The dominant sources of the latter are due to the spatial inhomogeneity of control fields or the intensity of control fields deviating from its nominal value. For instance, this error results from fluctuations in the Overhauser field in quantum dot systems [82,83]. In a doped crystal, the typical variation of the amplitude of the drive is about 20%–30% [81]. Hereafter, we use a dimensionless parameter ϵ_A to characterize the pulse area error, i.e.,

$$A \rightarrow A(1 + \epsilon_A). \quad (3)$$

Off-resonance effects, which refer to the mismatch between the control field frequency and the associated transition frequency, arise due the deviation from either of these frequencies. In practice, the transition frequency can be varied, for instance due to an energy level shift in atomic systems [84] or inhomogeneous broadening of the hyperfine levels in an ion-doped yttrium orthosilicate crystal [85,86]. Moreover, the control field frequency may also be altered on account of fluctuations in the external environment. In some integrated photonic circuits, off-resonance effects occur if the waveguides have distinct geometries

[87,88]. For the sake of description, we introduce the detuning error ϵ_Δ to represent off-resonance effects, i.e.,

$$\Delta \rightarrow \Delta + \epsilon_\Delta, \quad (4)$$

where $\Delta = 0$ means that the system is in the resonant regime.

It is worth noting that the major disadvantage of the resonant pulse is its high susceptibility to pulse area errors and off-resonance effects. To significantly enhance the robustness against both types of systematic errors, one can turn to the composite pulses [89–91], a train of pulses with identical amplitudes and relative phases to be addressed. The total evolution operator for the N pulse can be formulated as

$$\mathcal{U}_{\text{tot}} = \mathcal{U}(\theta_N)\mathcal{U}(\theta_{N-1}) \cdots \mathcal{U}(\theta_2)\mathcal{U}(\theta_1), \quad (5)$$

where $\mathcal{U}(\theta_n) = \exp[-iH(\theta_n)T]$ is the evolution operator of the n th pulse with pulse duration T and Hamiltonian $H(\theta_n)$, $n = 1, \dots, N$.

There are numerous methods to determine the value of the phase θ_n ($n = 1, \dots, N$). Among them, the most commonly used is to perform a Taylor expansion in the vicinity of the error $\epsilon = 0$ [92–99], which has been experimentally demonstrated in various physical platforms [100–103]. This method has its own limitation. Whereas the analytical solutions for the phases have been derived in several simple cases (e.g., a single type of error) [104–107], more often, the expressions of the Taylor expansion coefficients become particularly cumbersome for multiple types of systematic errors. As a result, even if the complicated expressions are given, only numerical solutions are accessible for the phases [108–111]. Worse still, sometimes the solutions may not exist, and thus one requires the aid of cost functions [112,113].

In this work, we ascertain the phase θ_n ($n = 1, \dots, N$) by training the samples using the supervised learning model, which can effectively settle the aforementioned issues. Not only that, this model can also solve problems that traditional composite pulses are incapable of handling, e.g., for time-varying errors [114–121]. For brevity, from now on, we adopt the vector θ to represent all phase parameters, i.e., $\theta = (\theta_1, \dots, \theta_N)$.

III. SUPERVISED LEARNING MODEL

A. Cost function

We begin by constructing the cost function for the supervised learning model. Given a set of training data $\{\mathbf{x}_k, y_k\}$, the goal of supervised learning is to learn a mapping from \mathbf{x} to y , where y_k is called the label or target of sample \mathbf{x}_k (usually a vector) in the data set. Here, the phases θ are the training parameters to be learned to make quantum control (operations) as immune to errors as possible.

In the absence of errors, one can also acquire perfect quantum operations by composite pulses. Nevertheless, the fidelity of quantum operations declines to varying degrees when exhibiting different types of errors. Under such circumstances, the fidelity of quantum operations can be regarded as a function of errors. Therefore, the samples in the training set come from various types of systematic errors, i.e.,

$$\mathbf{x}_k = \boldsymbol{\epsilon}_k = (\epsilon_k^1, \dots, \epsilon_k^\ell, \dots, \epsilon_k^L), \quad (6)$$

where L represents the highest dimension of samples, the subscript k denotes the k th sample, and the ℓ th component ϵ_k^ℓ ($\ell = 1, \dots, L$) characterizes a certain type (time interval) of systematic error.

More specifically, if systematic errors are unknown constants, different components of the sample represent different error types. For example, two components of the sample $\mathbf{x}_k = \{\epsilon_k^A, \epsilon_k^\Delta, \dots\}$ are the pulse area error ϵ_k^A and detuning error ϵ_k^Δ . If the systematic error belongs to one type of time-varying noise then different components of the sample represent the error in different time intervals, e.g., $\mathbf{x}_k = \{\epsilon_k^{A,t_1}, \dots, \epsilon_k^{A,t_\ell}, \dots\}$, where ϵ_k^{A,t_ℓ} denotes the k th sample of the pulse area error in the time interval $[t_\ell, t_{\ell+1}]$. Of course, one can utilize a mixture of different types and time intervals of errors to generate the samples, e.g., $\mathbf{x}_k = \{\epsilon_k^{A,t_1}, \dots, \epsilon_k^{A,t_\ell}, \dots, \epsilon_k^{\Delta,t_1}, \dots, \epsilon_k^{\Delta,t_\ell}, \dots\}$. In other words, the samples can be simultaneously drawn from both time-independent and time-dependent systematic errors to form a training set in this model.

The label we adopt here is the expected fidelity $\hat{F}(\mathbf{x}_k)$ of quantum operations,

$$y_k = \hat{F}(\mathbf{x}_k). \quad (7)$$

In the ideal situation, we naturally expect the system to be completely resistant to all errors. That is, $\hat{F}(\mathbf{x}_k) = 1$ for all samples \mathbf{x}_k , reflecting the ideal fact that quantum operations are still fully accurate in the presence of a variety of systematic errors.

For each sample \mathbf{x}_k , we define the loss function

$$\mathcal{L}_k = y_k - F(\mathbf{x}_k), \quad (8)$$

where $F(\mathbf{x}_k)$ is the actual fidelity of quantum operations when the system exhibits error $\boldsymbol{\epsilon}_k$ (equivalent to \mathbf{x}_k). Note that the expressions for $F(\mathbf{x}_k)$ rely on different quantum operations. For quantum state preparations, $F(\mathbf{x}_k)$ can be given by

$$F(\mathbf{x}_k) = |\langle \Psi_T | \Psi \rangle|^2, \quad (9)$$

where $|\Psi_T\rangle$ is the target state and $|\Psi\rangle$ is the final state of the system after performing composite pulses. With regard

to quantum gate operations, $F(\mathbf{x}_k)$ can be written as

$$F(\mathbf{x}_k) = \frac{1}{M} \text{tr}(\mathbf{U}_T^\dagger \mathcal{U}_{\text{tot}}), \quad (10)$$

where \mathbf{U}_T is the target quantum gate with M being its dimension, and \mathcal{U}_{tot} denotes the total evolution operator for composite pulses. Then, the cost function of the supervised learning model is defined by

$$J = \frac{1}{K} \sum_{k=1}^K \mathcal{L}_k = \frac{1}{K} \sum_{k=1}^K [y_k - F(\mathbf{x}_k)], \quad (11)$$

which represents the average of all loss functions, where K is the sample size. The phase parameters θ are trained in the direction that the cost function (11) decreases.

B. Robustness infidelity measure

In general, one training session on the samples does not necessarily lead to the solution we desire. Thus, performance evaluation for the solution (i.e., the phase parameters θ) is required to determine whether or not to stop the training procedure. To this end, we next introduce the definitions of fidelity and robustness.

Let us start with the case of one-dimensional error. Given a set of the phase parameters θ , the definition of the average fidelity \bar{F} is expressed by

$$\bar{F} = \int \rho(\epsilon) F_\theta(\epsilon) d\epsilon, \quad (12)$$

where $F_\theta(\epsilon)$ represents the fidelity of quantum operations obtained by using the phase parameters θ when the error is ϵ , and $\rho(\epsilon)$ is the probability density distribution of the error. In reality, it is difficult to exactly predetermine the specific distribution of $\rho(\epsilon)$. The usual way to tackle it is to use an *a priori* density distribution such as the uniform distribution or the Gaussian distribution. Here, $\rho(\epsilon)$ is simply taken to be a uniform distribution, i.e., all errors in the interval $[\epsilon_-, \epsilon_+]$ are considered equally weighted. Therefore, the form of $\rho(\epsilon)$ is

$$\rho(\epsilon) = \begin{cases} \frac{1}{\epsilon_+ - \epsilon_-}, & \epsilon \in [\epsilon_-, \epsilon_+], \\ 0, & \text{otherwise.} \end{cases} \quad (13)$$

As a result, Eq. (12) becomes

$$\bar{F}(\epsilon_-, \epsilon_+) = \frac{1}{\epsilon_+ - \epsilon_-} \int_{\epsilon_-}^{\epsilon_+} F_\theta(\epsilon) d\epsilon. \quad (14)$$

Its discrete version reads

$$\bar{F}(\epsilon_-, \epsilon_+) = \frac{1}{\epsilon_+ - \epsilon_-} \sum_j F_\theta(\epsilon_j) \Delta\epsilon_j. \quad (15)$$

Accordingly, we can define the average infidelity by

$$I_f(\epsilon_-, \epsilon_+) = \frac{1}{\epsilon_+ - \epsilon_-} \int_{\epsilon_-}^{\epsilon_+} [1 - F_\theta(\epsilon)] d\epsilon = 1 - \bar{F}(\epsilon_-, \epsilon_+). \quad (16)$$

In fact, Eq. (16) is also the definition of the first-order *robust-infidelity measure* (RIM) [122] following a uniform distribution. A small RIM indicates that the learned parameters make the system dynamics very robust and have high-fidelity quantum operations, while a large RIM signifies poor robustness and fidelity.

Although RIM can be used to quantify both robustness and fidelity for a set of learned parameters, it is difficult to intuitively benchmark how robust the learned parameters are from Eq. (16). To describe it more precisely, we define the robust width $W(\xi)$ as

$$W(\xi) = \epsilon_{\max} - \epsilon_{\min}, \quad (17)$$

where all errors in the interval $[\epsilon_{\min}, \epsilon_{\max}]$ satisfy

$$\max\{1 - F_\theta(\epsilon)\} \leq \xi, \epsilon \in [\epsilon_{\min}, \epsilon_{\max}] \quad (18)$$

with a given threshold ξ . It is clear that a large (small) $W(\xi)$ means high (poor) robustness. Remarkably, these definitions can be easily generalized to the case of multidimensional errors.

C. Training and testing

Given the cost function (11), we train the phase parameters to yield its minimum value, and then test the robust performance for the learned phase parameters according to Eq. (14). The learning procedure is divided into two steps: *training* and *testing*.

In the *training stage*, we first specify a training set by drawing K samples from errors through several common probability distributions, such as the Gaussian distribution, the uniform distribution, the beta distribution, and the exponential distribution. Once the training set of K samples is obtained, we evaluate the cost function J given by Eq. (11) via a random set of initial phase parameters, and then update the phase parameters using the modified gradient descent algorithm, which is introduced in the next section. The cost function J gradually diminishes with the passage of iterations, and the training does not end until either the optimal value is obtained or a certain threshold of this cost function is reached.

In the *testing stage*, we apply the phase parameters learned from the training stage to assess the robust performance for this composite pulse sequence using the average fidelity. Specifically, we first calculate the fidelity $F_\theta(\epsilon)$ for all possible errors rather than resampling them, and then the average fidelity $\bar{F}(\epsilon_-, \epsilon_+)$ in the interval $[\epsilon_-, \epsilon_+]$

according to Eq. (14). When the average fidelity reaches the expected value, we accept the learned phase parameters and terminate the whole learning procedure. Otherwise, the learning procedure is a failure and we must retrain the phase parameters to obtain another solution, i.e., returning to the training stage with a new set of samples or initial phase parameters.

In Fig. 1, the blue dots represent the samples in the training set. Note that all blue dots have a value of 1, which implies that the quantum operation we desire is perfect however large the systematic errors. The green rhomboids are the actual fidelities of the samples, and their positions vary depending on the values of phase parameters. The red dotted curve (hypersurface) is plotted according to the phase parameters learned from the training stage, and each point on the curve (hypersurface) corresponds to the actual

fidelity of the quantum operation at specific values of the systematic errors.

From a physical point of view, the closer the curve (hypersurface) is to the line $\hat{F}(\epsilon) = 1$ [the hyperplane $\hat{F}(\epsilon^1, \dots, \epsilon^\ell, \dots, \epsilon^L) = 1$], the less susceptible the quantum operation is to errors. Obviously, the shapes of the curves (hypersurfaces) are quite different for distinct phase parameters, and the objective is to attain an optimal solution of the phase parameters θ by training these rhomboids in Fig. 1.

D. Modified gradient descent algorithm

In the original GRAPE algorithm [64], the control variables are *amplitudes* of control fields, but they become *phases* here. As a result, the original GRAPE algorithm cannot be directly applied in the current model, and a modified version is urgently required to accommodate this situation. We next explain the details of this modified GRAPE algorithm.

At first, we need to rewrite the Hamiltonian of the n th pulse as ($n = 1, \dots, N$)

$$\begin{aligned} H(\theta_n) &= e^{-i\theta_n} \sigma_+ + e^{i\theta_n} \sigma_- \\ &= \cos \theta_n \sigma_x + \sin \theta_n \sigma_y \\ &= u_{n,x} H_x + u_{n,y} H_y, \end{aligned} \quad (19)$$

where $H_{x(y)} = \sigma_{x(y)}$, and Ω is regarded as a unit. In Eq. (19), two virtual variables $u_{n,x}$ and $u_{n,y}$ are exploited to substitute for the phase parameter θ_n , and they satisfy the relation

$$\theta_n = \arctan \frac{u_{n,y}}{u_{n,x}}. \quad (20)$$

After this substitution, we can use the gradient descent algorithm to update the virtual variables $u_{n,x}$ and $u_{n,y}$, i.e.,

$$u'_{n,x} = u_{n,x} - \alpha_x \frac{\delta J}{\delta u_{n,x}}, \quad (21)$$

$$u'_{n,y} = u_{n,y} - \alpha_y \frac{\delta J}{\delta u_{n,y}}, \quad (22)$$

where both α_x and α_y are some prescribed step sizes. Then, the new phase parameter in the next iteration reads

$$\theta'_n = \arctan \frac{u'_{n,y}}{u'_{n,x}}. \quad (23)$$

It is worth stressing that $u_{n,x}$ and $u_{n,y}$ are only introduced as a mathematical tool, and they do not have to possess physical meaning. Figure 2 illustrates the geometric interpretation of the gradient descent principle. Here, the updated formulas for the phases given by Eqs. (20)–(23)

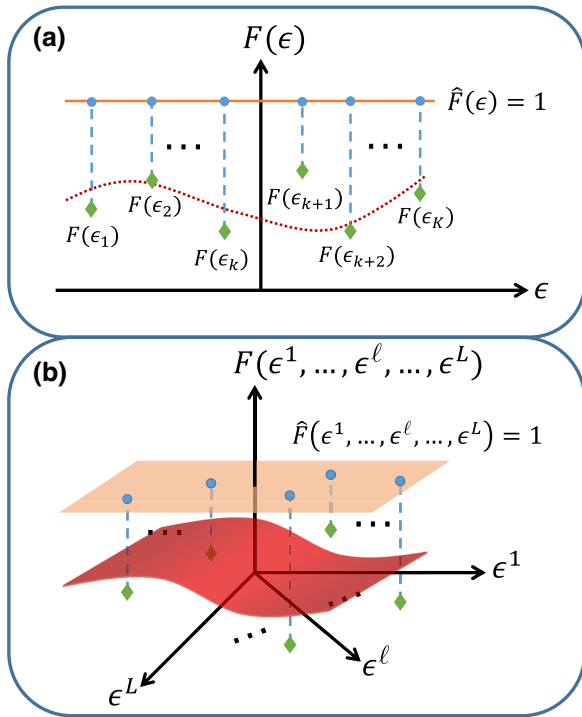


FIG. 1. Schematic diagram of the data space. (a) Two-dimensional space composed of error ϵ and fidelity $F(\epsilon)$, where the filled circles and rhomboids represent the expected and actual sample fidelities, respectively. According to the labeled training set $\{\epsilon_k, \hat{F}(\epsilon_k)\}$, the phase parameters θ are trained so that the red dotted curve fit by the data points is as close as possible to the orange solid line, where $k = 1, \dots, K$ with K the sample size. (b) The $(L + 1)$ -dimensional space, where the L -dimensional hyperplane $\hat{F}(\epsilon^1, \dots, \epsilon^\ell, \dots, \epsilon^L) = 1$ represents an ideal situation in which the fidelity of quantum operations is completely unaffected by all types (time intervals) of errors. We have to train the phase parameters θ so that the red hypersurface fit by the filled rhomboids approaches as much as possible the orange hyperplane $\hat{F}(\epsilon^1, \dots, \epsilon^\ell, \dots, \epsilon^L) = 1$.

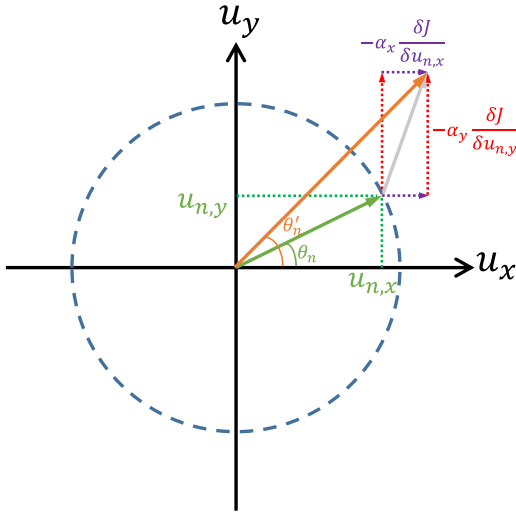


FIG. 2. Geometric interpretation of the modified GRAPE algorithm. First, the phase θ_n ($n = 1, \dots, N$) is mapped onto the unit circle to yield a unit vector (the green line). By orthogonal decomposition of this vector, we obtain two variables $u_{n,x}$ and $u_{n,y}$. Then, we use the gradient descent algorithm to calculate the increment in both directions, and thus acquire the increment vector (the gray line). According to the parallelogram law of vectors, we obtain a new vector (the orange line) whose direction is actually the gradient descent direction. As a result, we have the new phase θ'_n in the next iteration. The iteration process continues until the gradient threshold is reached. For detailed steps, see Algorithm 1.

are quite different from those proposed in Ref. [123]. Specifically, we evaluate the gradient of the cost function with the aid of two types of virtual variables, while the gradient with respect to the phase is directly calculated after performing the rotating-wave approximation in a rotating frame in Ref. [123].

It is important to note that the modified GRAPE algorithm is very crude, not because we cannot find a solution of the training parameters θ , but because there are very many locally optimal solutions. To search global optimal solutions of the training parameters (probably more than one), two common methods of “escaping” or “restarting” are usually adopted, namely, randomly searching the neighborhood of the current solution in parameter space, or ignoring the current solution, and exploring a new one in

ALGORITHM 1. Modified GRAPE algorithm.

1. Randomly input the initial phase parameters θ_n .
2. Calculate the virtual variables $u_{n,x} = \cos \theta_n$ and $u_{n,y} = \sin \theta_n$.
3. Evaluate the increments and update the virtual variables, labeled as $u'_{n,x}$ and $u'_{n,y}$.
4. Calculate the parameters $\theta'_n = \arctan u'_{n,y} / u'_{n,x}$.
5. Regard the θ'_n as new phase parameters.
6. Go to step 2 until the threshold is reached.

parameter space. Here, we adopt the latter method, which can take full advantage of parallel training to improve computational efficiency. Specifically, we use a large enough number of training groups, with each group trained individually. After accomplishing the training, we measure the performance of each group using the average fidelity defined by Eq. (14). Then, the phase parameters that make the average fidelity reach the desired value are left, and the rest are simply discarded. As for the former, we can introduce the simulated annealing method into the modified GRAPE algorithm, similar to that used in Refs. [124,125]. For details, we refer the reader to Appendix A.

E. Sampling methods

In the current model, one of the most important parts is to acquire enough representative samples. If the sample size is too small, it is easy to observe underfitting, where the parameter law of the model may not be well learned. How to efficiently draw enough samples becomes very critical in supervised learning. In particular, the usage of different training samples will produce different solutions of training parameters, and such discrepancies can significantly impact the quality of robust quantum control.

Figure 3 shows the relationship between the average infidelity $I_f(-0.3, 0.3)$ and the total number of samples, where the objective is to achieve population inversion in a robust manner, and the samples come from the pulse area error given by Eq. (3). For cases in which the sample size is particularly large, we split them into multiple groups for independent training, and then pick out the optimal solutions from these groups. The purpose of this is that we can

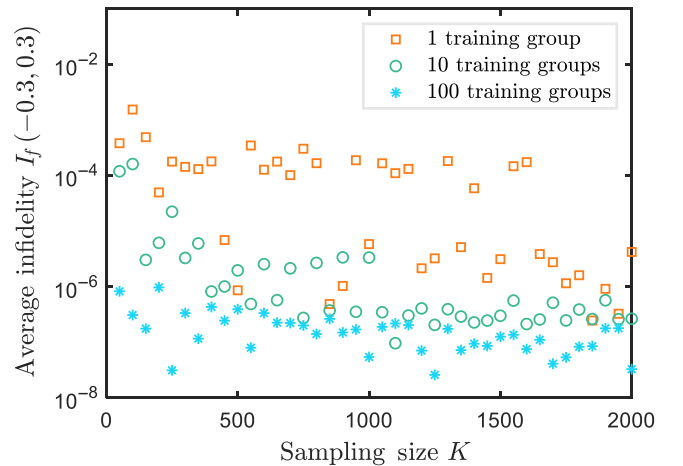


FIG. 3. Average infidelity $I_f(-0.3, 0.3)$ versus the sampling size K . The objective is to robustly attain population inversion in the presence of the pulse area error, where we uniformly draw the samples from the interval $[0, 0.3]$, set the pulse area of each pulse to $\pi/2$, choose the pulse number $N = 7$, adopt a step size of 0.001, and randomly select initial values of the training parameters θ from the range $[-\pi, \pi]$.

train the parameters in parallel, thus improving the computational efficiency. It is readily found that the average infidelity is relatively large and oscillates when the sample size K is not large enough. With increasing sampling size, the average infidelity gradually decreases and stabilizes at a relatively low level. This implies that having sufficient samples is imperative for successfully training the parameters. Furthermore, increasing the number of training groups also facilitates parameter training, making it easier to find the optimal solutions.

We next investigate the influence of different sampling distributions on the robust performance of quantum control. We plot in Fig. 4(a) the robust performances of population inversion for various learned phase parameters θ , which have been trained by several common sampling distributions, including the uniform distribution $U(\epsilon_-, \epsilon_+)$ with sampling interval $[\epsilon_-, \epsilon_+]$, the Gaussian distribution $G(\mu, \nu)$ with expectation μ and variance ν , the exponential distribution $E(\lambda)$ with rate parameter λ , and the beta distribution $B(\alpha, \beta)$ with parameters α and β . The specific expressions are given in Appendix B and the

corresponding probability density functions are plotted in Fig. 4(b).

An inspection of Fig. 4(a) shows that the infidelity is mostly much less than 10^{-4} in the vicinity of the pulse area error $\epsilon = 0$ for all sampling distributions, indicating the success of these trainings. A closer look at Fig. 4(a) reveals that different sampling distributions lead to different robust performances of population inversion. For example, the phase parameters learned via the exponential distribution $E(0.3)$ have very good robustness with respect to errors, e.g., see the robust width $W(\xi)$ with the threshold ξ being 10^{-2} in Fig. 4(a). Nevertheless, the fidelity is not particularly high in the presence of errors when compared to other distributions. The reason behind these results is that, for the exponential distribution, we consider a small amount of samples with large magnitude, as shown in Fig. 4(b).

On the contrary, the fidelity is high in the presence of errors with small magnitude, but the robust width is not very large for the uniform distribution $U(0, 0.3)$. Therefore, during the training process, the samples with small magnitude promote high fidelity, while the samples with large magnitude promote robustness.

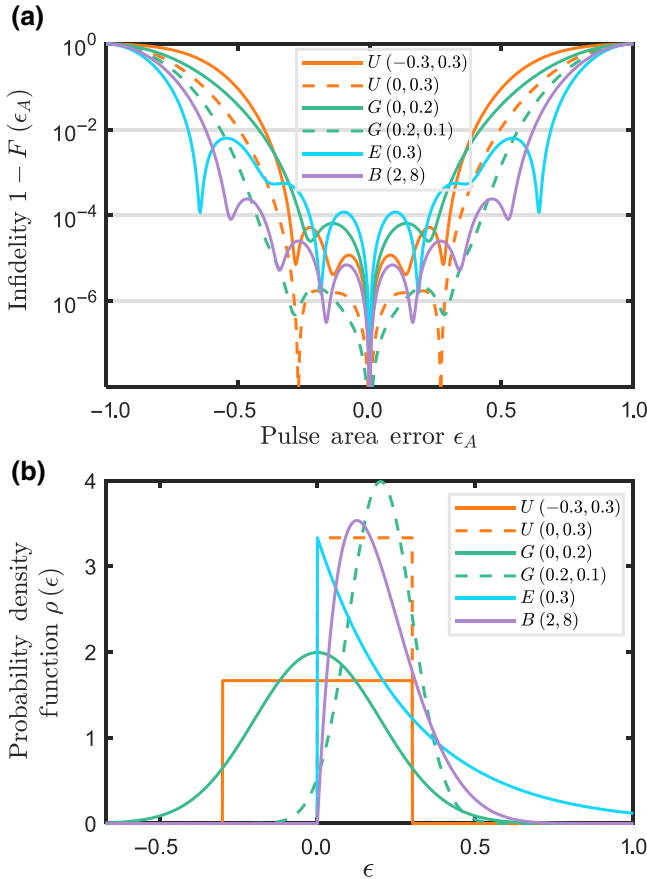


FIG. 4. (a) Infidelity $1 - F(\epsilon_A)$ of population inversion versus the pulse area error ϵ_A by using different sampling distributions. The learned phase parameters are given in Table I. (b) Probability density function for different distributions.

F. Generalization ability

The generalization ability is a key indicator to measure the quality of supervised learning models. It refers to the ability to generalize from the training set to the testing set. Generally speaking, the supervised learning model possesses strong generalization ability when executing well in predicting samples that have never been seen before. For learned phase parameters θ , the generalization ability can be quantified by the average infidelity $I_f(\epsilon_-, \epsilon_+)$ in Eq. (16). Specifically, a strong generalization ability is reflected in a small average infidelity $I_f(\epsilon_-, \epsilon_+)$, while a large $I_f(\epsilon_-, \epsilon_+)$ indicates that the fidelity of quantum control is not very high and also has poor robustness with respect to the errors. Note that the average infidelity $I_f(\epsilon_-, \epsilon_+)$ is difficult to accurately characterize within what error range the learned phase parameters θ have strong robustness. Therefore, we adopt the robust width $W(\xi)$ in Eq. (17). Apparently, the robustness is better if $W(\xi)$ is larger.

Figure 5(a) shows the average infidelity of population inversion as a function of the sampling boundary for different pulse numbers, where the samples are uniformly drawn from the interval $[0, \epsilon'_+]$ with the prime notation added to ϵ_+ to distinguish the sampling boundary from the error boundary. We can observe that the average infidelity is particularly small when the sampling range is small; see $\epsilon'_+ < 0.2$. This indicates that the generalization ability is very strong within the small sampling range. As the sampling boundary increases, the average infidelity

TABLE I. Learned phase parameters θ in Figs. 4–10 and Videos 1 and 2 below. We set the pulse area of each pulse to $\pi/2$, adopt a step size of 0.001, train 500 groups of samples with a sample size of $K = 1000$, and randomly select the initial values of the phase parameters θ from the range $[-\pi, \pi]$.

	Distribution	N	θ_1	θ_2	θ_3	θ_4	θ_5	θ_6	θ_7	θ_8	θ_9
Figure 4	$U(-0.3, 0.3)$	7	1.1349	0.3521	-1.8097	2.3882	-1.4894	-2.2752	2.9204		
Figure 4	$U(0, 0.3)$	7	-0.0890	-0.0883	2.8061	1.8183	0.3086	-1.7302	0.9139		
Figure 4	$G(0, 0.2)$	7	0.3267	-2.2901	1.7353	-1.4601	-1.3068	-2.7500	-0.3568		
Figure 4	$G(0.2, 0.1)$	7	-1.1718	-1.6562	2.9098	0.2857	2.8737	-1.9269	-0.9110		
Figure 4	$E(0.3)$	7	-1.7314	-0.9706	-0.0454	2.3807	0.0650	-1.3612	-1.5465		
Figure 4	$B(2, 8)$	7	1.2869	0.8791	-0.6698	3.1261	-0.6310	0.6509	1.4951		
Figure 6	$U(0, 0.3)$	5	2.8622	2.4234	0.0425	0.6872	-0.8656				
Figure 6	$U(0, 0.5)$	7	1.1002	2.7012	1.4171	-1.9374	0.9740	1.8036	-0.2582		
Figure 6	$U(0, 0.6)$	9	0.7598	1.1145	-0.8872	-0.0167	-1.5056	0.4233	-0.0248	2.9724	-3.0918
Figure 7	$U(-0.1, 0.3)$	9	1.1516	0.3675	-2.2800	0.5743	2.0933	0.2061	-1.6437	-0.7061	0.9273
Figure 8	$U(-0.25, 0)$	9	0.6220	0.6251	1.1929	1.6412	-0.8985	-1.5013	-0.5969	-0.6176	1.2448
Figure 8	$U(-0.15, 0.15)$	9	2.7879	1.8734	-2.8629	1.2522	2.4905	-1.1821	-1.8967	-2.1757	2.4733
Figure 8	$U(0, 0.25)$	9	-2.8126	-2.7701	-1.0354	-2.8256	2.3944	-1.7776	-0.7125	0.5963	-1.4869
Figure 9(a)	$U(0, 0.22)$	7	1.8826	-0.5939	0.1365	-1.2262	-1.8446	1.7622	2.2986		
Figure 9(b)	$U(0, 0.22)$	9	-1.2035	1.7050	2.0577	-0.7816	0.7853	-1.3623	0.9122	0.0378	2.7522
Figure 10	$G(0.1, 0.02)$	5	1.2993	1.5066	-0.4582	1.6285	2.6998				
Video 1	$U(-0.1, 0.3)$	7	2.2802	2.6146	0.0101	-0.3657	0.9080	-2.3146	1.3232		
Video 2	$U(-0.1, 0.3)$	7	1.8992	2.4589	-0.023	-0.577	0.5731	2.5166	0.1152		

tends to increase on the whole, signifying that a large sampling range is not conducive to obtaining high fidelity of quantum operations.

In Fig. 5(b), we show the relationship between the robust width $W(\xi)$ and the sampling boundary ϵ'_+ , where the threshold ξ is equal to 10^{-4} . First, within a small sampling boundary, e.g., $\epsilon'_+ < 0.2$ in Fig. 5(b), there is not much improvement in the robust width when increasing the pulse number or sampling range, implying that the phase parameters are not properly trained. This is mainly due to the fact that the sampling range is too narrow to effectively represent all errors. As a result, although complex models may possess strong generalization ability, they are overlearning on the training set. To avoid this, we can either expand the sampling range or change the sampling method [e.g., employing the Gaussian distribution to consider a small amount of errors (samples) with large magnitude].

For a given pulse number, the robust width mainly exhibits a positive correlation when increasing the sampling range; see Fig. 5(b). While the sampling boundary exceeds a certain threshold, the robust width drops sharply, because the average infidelity becomes relatively large in such circumstance. Finally, the threshold of the sampling range varies depending on the number of pulses; see ϵ'_5, ϵ'_7 , and ϵ'_9 in Fig. 5(b). In particular, increasing the pulse number leads to an increase in both the threshold range and robust width.

Therefore, there is a trade-off between high fidelity and strong robustness at a given number of pulses in our model, because both the average infidelity and the robust width grow when increasing the sampling range; see Figs. 5(a) and 5(b). High fidelity usually leads to a reduction in robust

width, and vice versa. Thereby, for a specific number of pulses, an appropriate sampling range favors balancing high fidelity and a large robust width.

To simultaneously promote fidelity and robustness for quantum control, a feasible way is to increase the pulse number such that more phase parameters are involved during the training. The reason is that the rule to be learned is already known in the current model, i.e., the hyperplane $\hat{F}(\epsilon^1, \dots, \epsilon^\ell, \dots, \epsilon^L) = 1$ in Fig. 1(b). This is a little different from traditional supervised learning [126] in which the rule also needs to be learned in training. In some sense, our model can also be regarded as a multiple linear regression, where the surfaces made up of training samples and learned by researchers differ from the traditional ones. To be specific, in traditional supervised learning, the shape composed from training samples is usually a complicated hypersurface, and one always intends to fit it with a simple hyperplane determined by learned parameters. Here, a simple hyperplane is formed by the training samples $\{\epsilon_k, \hat{F}(\epsilon_k)\}$, and we specify a hypersurface by training physical parameters to fit the hyperplane. In particular, the more phase parameters, the closer the hypersurface will be to the hyperplane.

IV. APPLICATIONS: ROBUST QUANTUM CONTROL

A. Single type of error

We begin by illustrating a scenario in which the system exhibits only one type of error. That is, the samples are one dimensional. Indeed, we have explained in detail in Sec. II how to successfully train the phase parameters θ

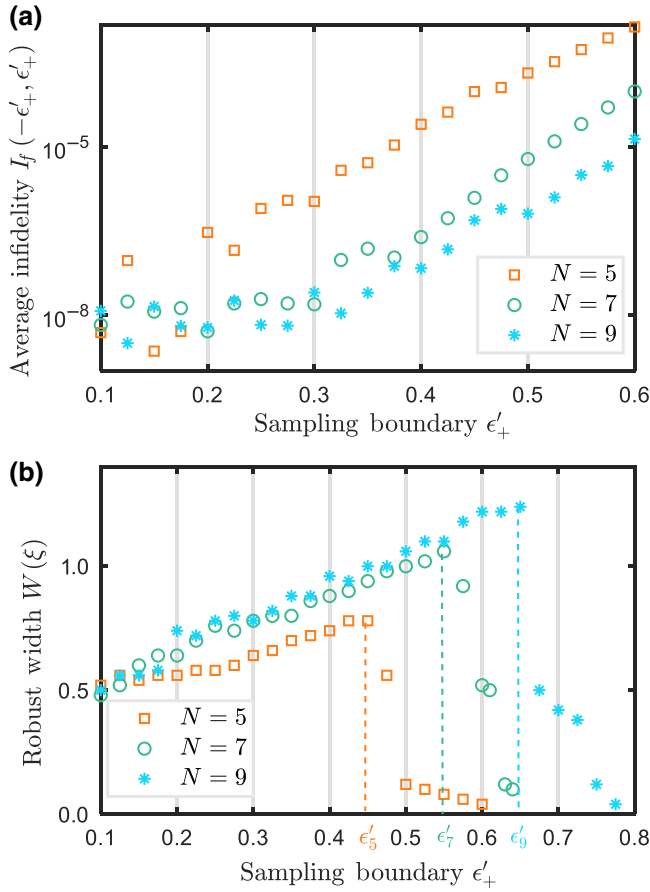


FIG. 5. (a) Average infidelity $I_f(-\epsilon'_+, \epsilon'_+)$ and (b) robust width $W(\xi)$ versus the sampling boundary ϵ'_+ for different pulse numbers N . The objective and the parameters are the same as in Fig. 3.

to achieve robust population inversion in the presence of the pulse area error ϵ_A given by Eq. (3). We now demonstrate that this model is equally applicable to suppressing the influence of other types of errors, such as the detuning error ϵ_Δ given by Eq. (4).

Figure 6 shows the infidelity of population inversion in the presence of detuning error by the learned phase parameters, where the samples ϵ_k^Δ are drawn from the uniform distribution $U(0, 0.3)$. The ultralow infidelity ranges reveal that it is also feasible to make the system robust with respect to detuning error by training on the phase parameters. Furthermore, the robustness becomes stronger as the number of pulses increases, as also indicated in Fig. 6.

1. Arbitrary superposition states

So far, the supervised learning model is merely illustrated to realize robust population inversion. Actually, this model is suitable for implementing arbitrary population transfer in a robust manner as well. To this end, it is imperative to transform the target state into a superposition state

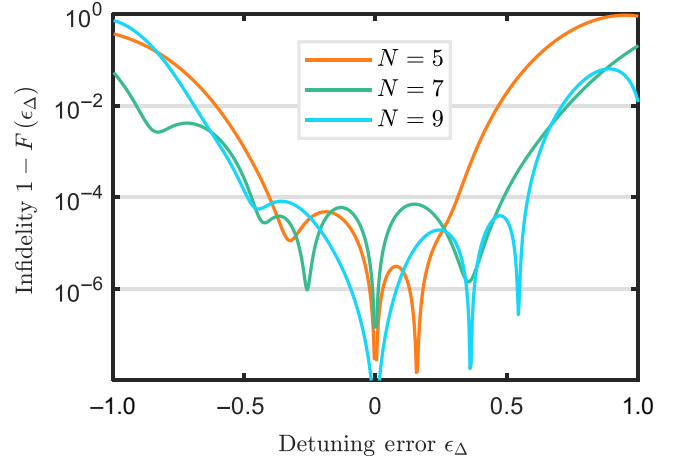


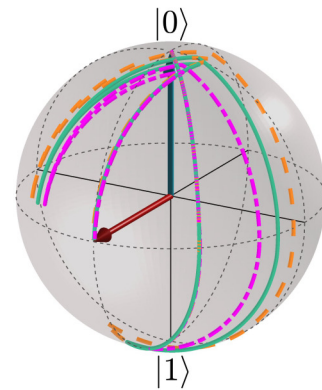
FIG. 6. Infidelity $1 - F(\epsilon_\Delta)$ of population inversion versus the detuning error ϵ_Δ for different pulse numbers N . Each profile is plotted according to the learned phase parameters θ offered in Table I.

we desire to prepare, whose general form is given by

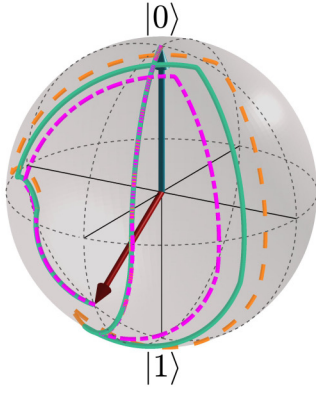
$$|\psi_T\rangle = \cos \phi |0\rangle + e^{i\varphi} \sin \phi |1\rangle, \quad (24)$$

where ϕ and φ can be arbitrary. After establishing the target state, we then employ Eq. (9) to train the phase parameters to accomplish this goal.

Videos 1 and 2 show the time-evolution trajectories for robust preparation of different superposition states through the learned phase parameters θ . We can see that, when the system exhibits pulse area error, the trajectories (the dashed and dash-dot curves) gradually deviate from the exact one (the solid curve) during the evolution process. Despite this, these three trajectories eventually come



VIDEO 1. Visualization of robustly preparing the superposition state $(|0\rangle + |1\rangle)/\sqrt{2}$ on the Bloch sphere. The learned phase parameters θ are presented in Table I, and the blue (red) arrow denotes the Bloch vector pointing to the initial (final) state. The solid, dashed, and dash-dot curves represent the evolution trajectories of the system state in the presence of the pulse area error $\epsilon_A = 0, +0.1, \text{ and } -0.1$, respectively.



VIDEO 2. Visualization of robustly preparing the superposition state $(|0\rangle + \sqrt{3}|1\rangle)/2$ on the Bloch sphere. The learned phase parameters θ are given in Table I.

together. Therefore, the learned phase parameters θ do ensure that the target state $|\psi_T\rangle$ is still obtained with an ultrahigh fidelity even in the presence of systematic errors.

2. General single-qubit gates

This supervised learning model can be used not only to prepare arbitrary superposition states, but also to implement general single-qubit gates. The expression for a general single-qubit gate can be written as

$$\mathbf{U}(\phi, \varphi, \Phi) = \begin{bmatrix} e^{i\Phi} \cos \phi & -e^{-i(\varphi+\Phi)} \sin \phi \\ e^{i(\varphi+\Phi)} \sin \phi & e^{-i\Phi} \cos \phi \end{bmatrix}, \quad (25)$$

where ϕ , φ , and Φ are arbitrary real numbers based on the desired quantum gate. In the current model, there are two methods to robustly obtain the general single-qubit gate given by Eq. (25). Next, we present the details of these two methods.

(i) *State-based method.* Given that the initial state of the system is $|0\rangle$, we first train the phase parameters θ to robustly obtain a superposition state $|\psi_T\rangle = \cos \phi|0\rangle + e^{i\varphi} \sin \phi|1\rangle$, where the values of ϕ and φ are determined by the desired quantum gate. Then, we shift the learned phase parameters by an appropriate angle:

$$\theta \leftarrow \theta + \Phi \quad (26)$$

with the shift angle Φ dependent on the desired quantum gate as well. We emphasize that this phase shift manipulation does not change the probability amplitude of the matrix elements in Eq. (25); rather, it modifies only the relative phase between different matrix elements. Therefore, the final learned phase parameters for implementing the general single-qubit gate in a robust manner become $\theta + \Phi$. As an example, the learned phase parameters θ adopted in Video 1 can also be used to implement the Hadamard gate with a specific phase that can be properly modulated by the phase shift Φ .

(ii) *Evolution operator-based method.* We directly solve the Schrödinger equation for the evolution operator $\mathcal{U}(t)$ of this system,

$$\dot{\mathcal{U}}(t) = -iH(t)\mathcal{U}(t), \quad (27)$$

where $H(t)$ is the system Hamiltonian, and $\mathcal{U}(0) = \mathbb{I}$ is an identity operator at the initial time. The target quantum gate $\mathbf{U}(\phi, \varphi, \Phi)$ can now be received via the evolution operator after N pulses, i.e.,

$$\mathcal{U}(NT) = \mathbf{U}(\phi, \varphi, \Phi). \quad (28)$$

In this situation, we adopt Eq. (10) to calculate the corresponding gradients.

Suppose now that we intend to execute a Hadamard gate:

$$\mathbf{H} = \frac{1}{\sqrt{2}} \begin{bmatrix} 1 & 1 \\ 1 & -1 \end{bmatrix}. \quad (29)$$

To this end, we proceed to train the phase parameters θ by minimizing the cost function given in Eq. (11). Figure 7 shows the variation of tomography results for the evolution operator $\mathcal{U}(NT)$ at different iterations during the training stage. We can see that the evolution operator of the system gradually approaches the Hadamard gate as the number of iterations increases, and eventually reaches the goal with ultrahigh fidelity.

Different from the case of population inversion, the robust performance of quantum gates is strongly correlated with the sampling distribution here. In other words, when training on the samples with different ranges, we learn different phase parameters. These phase parameters exhibit different robust performances for systematic errors.

In Fig. 8, we plot the infidelity of the Hadamard gate versus the pulse area error using various phase parameters that are learned from the training set drawn from distinct sampling ranges. It is clearly shown that the learned phase parameters manifest varying degrees of robustness to the pulse area error under different sampling distributions.

B. Multiple types of errors

When the system simultaneously exhibits different types of errors (e.g., pulse area and detuning errors), it is also convenient to employ this model to implement robust quantum control. In such a situation, the sample space becomes multidimensional, where each dimension represents a specific type of error. As a result, the training set can be represented as $\{\epsilon_k^A, \epsilon_k^\Delta, \dots, \hat{F}(\epsilon_k^A, \epsilon_k^\Delta, \dots)\}$, where $\hat{F}(\epsilon_k^A, \epsilon_k^\Delta, \dots) = 1$, $k = 1, \dots, K$. In Fig. 9, we plot the fidelity of population inversion as a function

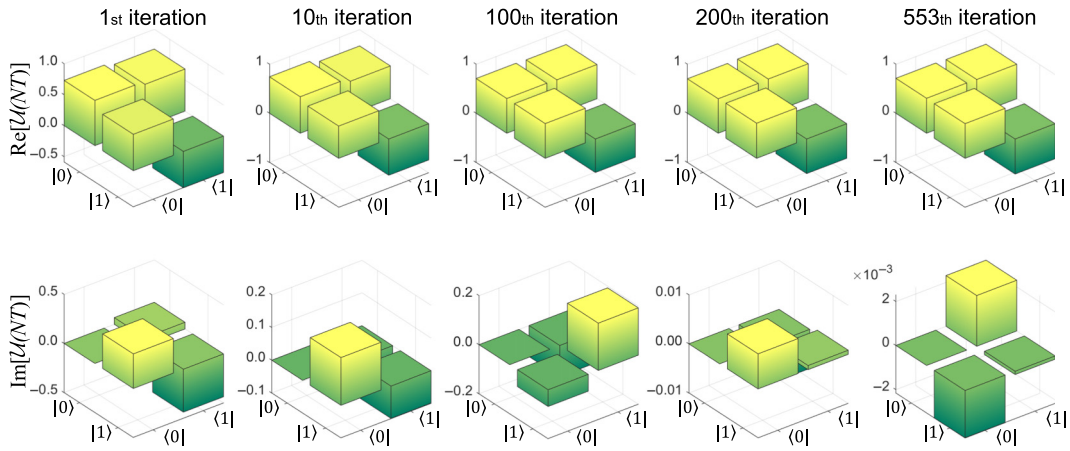


FIG. 7. Real and imaginary parts of the evolution operator $\mathcal{U}(NT)$ at different iterations during the training process. The objective is to robustly implement the Hadamard gate given in Eq. (29); the learned parameters are given in Table I.

of the pulse area and detuning errors by training different numbers of phase parameters. The results demonstrate that the training methodology is able to maintain its efficacy even when confronted with multiple types of errors.

C. Time-varying errors

In this section, we manage to train the phase parameters when the errors are time dependent. It is worth mentioning that one rarely obtains the exact Taylor series expression for time-varying errors by using traditional composite pulse technologies [127], because the Hamiltonian generally cannot commute with itself at different times. The popular method of tackling time-varying errors is to make use of an appropriate unitary transformation to formally divide the evolution operator of the system into error-free

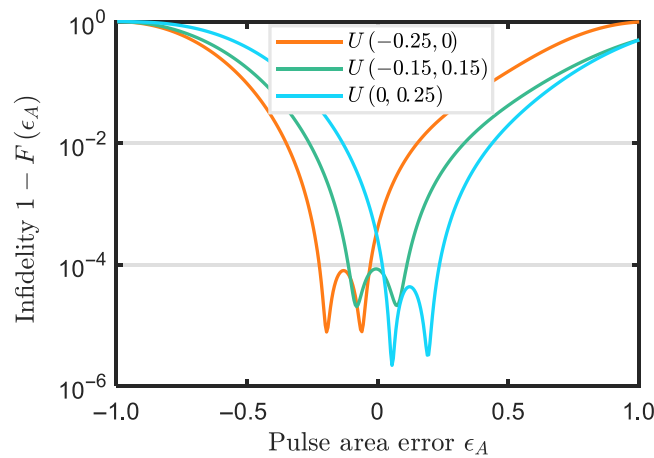


FIG. 8. Robust performances for the phase parameters θ learned from different ranges of the uniform distribution. The objective is the same as in Fig. 7, and the learned parameters are given in Table I.

and error terms, and then design related parameters to minimize the influence of the error term [128–134]. While this method is effective, it is quite cumbersome.

Here we show that it is still feasible to use the supervised learning model to address the case of time-varying errors. To this end, the training set needs to be modified

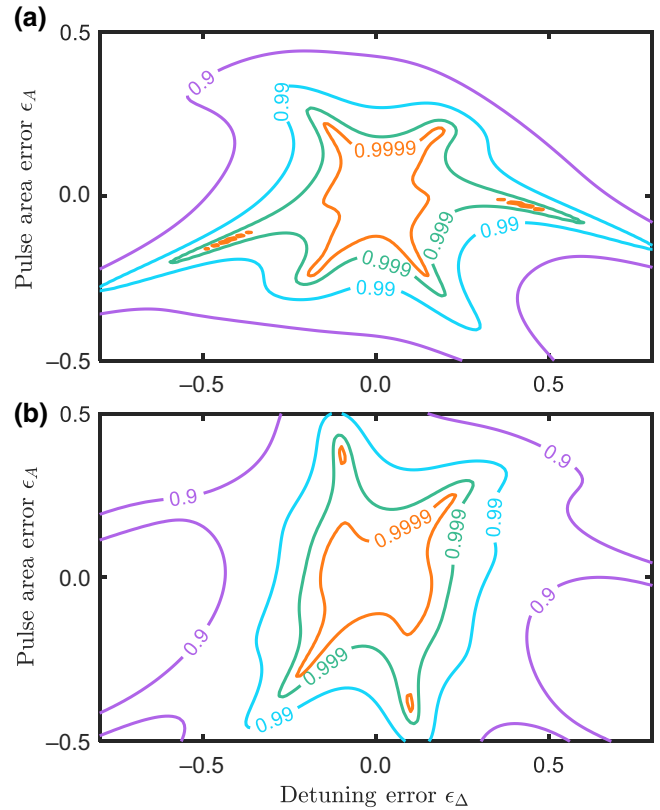


FIG. 9. Fidelity $F(\epsilon_A, \epsilon_\Delta)$ of population inversion versus the pulse area error ϵ_A and detuning error ϵ_Δ for different pulse numbers: (a) $N = 7$, (b) $N = 9$. The learned parameters are given in Table I.

as $\{\epsilon_k^{t_1}, \dots, \epsilon_k^{t_L}, \hat{F}(\epsilon_k^{t_1}, \dots, \epsilon_k^{t_L})\}$, where $\hat{F}(\epsilon_k^{t_1}, \dots, \epsilon_k^{t_L}) = 1$, and $\epsilon_k^{t_\ell}$ denotes the error magnitude in the time interval $[t_\ell, t_{\ell+1}]$, $\ell = 1, \dots, L$, $k = 1, \dots, K$. Namely, the time-dependent nature of errors is reflected in distinct dimensions of the samples.

Unlike the case of time-independent errors, it is difficult to account for all time-varying errors in the testing stage. To validate the phase parameters θ learned from the training stage, we randomly draw enough testing samples from time-varying errors for different time intervals. The fidelity of each testing sample is plotted in Fig. 10(a). It is clearly shown that the learned phase parameters θ perform very well in the vast majority of testing samples, where a total average fidelity of 99.55% is achieved. Furthermore, we demonstrate in Fig. 10(b) how to successfully obtain robust population inversion when the pulse area error suffers from time-dependent Gaussian noises. For a comparison, Fig. 10(b) also shows the fidelity as a function of the time-independent errors using the learned

phase parameters. We can observe that the robustness with respect to time-independent errors is much better than that of time-varying errors.

V. FURTHER EXTENSIONS

A. Training of detuning parameters

Up to now, we have regarded the phases as training parameters in the supervised learning model. Actually, the phases do not have unique specifications, and thus other physical parameters (e.g., detunings or Rabi frequencies) are also able to serve as training parameters instead. In the following, we investigate the feasibility of utilizing the detuning Δ_n ($n = 1, \dots, N$) of each pulse as training parameters to implement robust quantum control. Undoubtedly, the training of Rabi frequencies can be accomplished as well through a comparable procedure. To simplify the notation, all detunings Δ_n are collectively represented by a vector $\mathbf{\Delta}$, i.e., $\mathbf{\Delta} = (\Delta_1, \dots, \Delta_N)$.

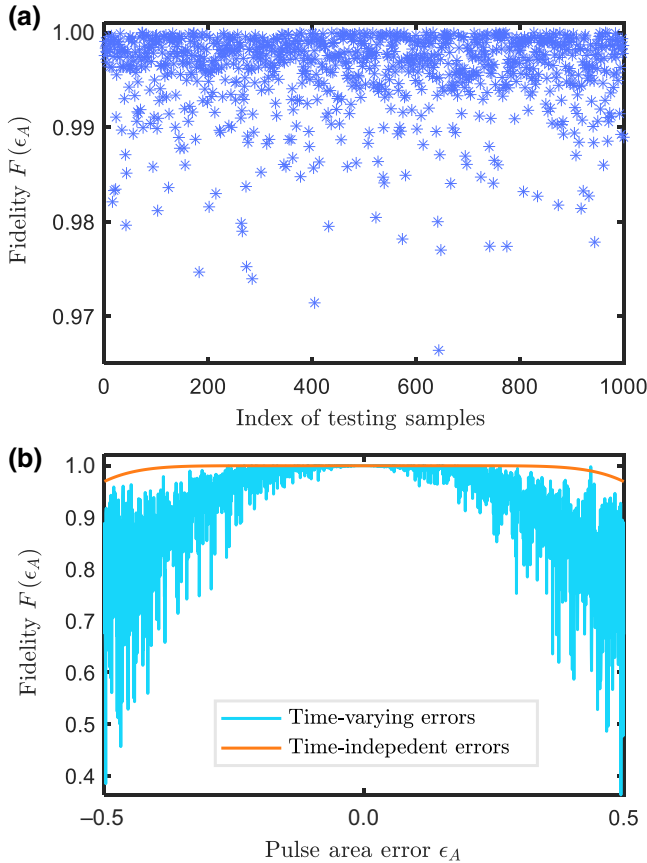


FIG. 10. (a) Testing performance for the learned phase parameters θ , where the average fidelity of population inversion is about 99.55% for 1000 testing samples. The time interval is $t_{\ell+1} - t_\ell = T$, with the other parameters given in Table I. (b) Fidelity $F(\epsilon_A)$ of population inversion versus the pulse area error ϵ_A , where the pulse area error suffers from time-dependent Gaussian noises with expectation $0.1\epsilon_A$ and variance $0.1\epsilon_A$.

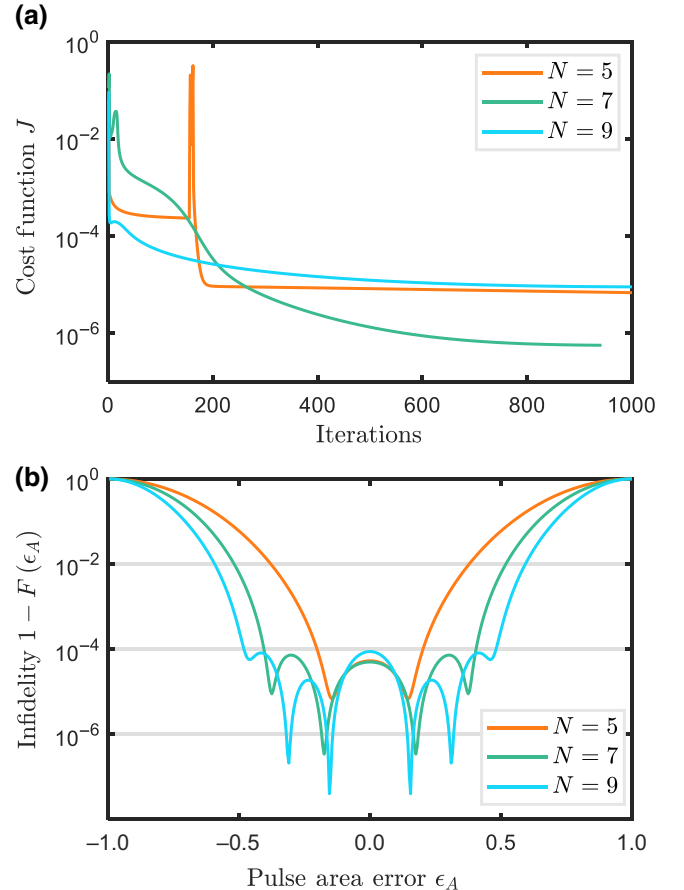


FIG. 11. (a) Cost function versus the number of iterations for different numbers of detuning parameters. The sudden increase in the cost function is due to the reinitialization of the large detuning. (b) Infidelity $1 - F(\epsilon_A)$ of population inversion versus the pulse area error ϵ_A by using distinct learned detuning parameters $\mathbf{\Delta}$ given in Table II.

TABLE II. Learned detuning parameters Δ used in Fig. 11. We set the duration of each pulse to $T_n = \pi/(2\sqrt{\Omega_n^2 + \Delta_n^2})$, adopt a step size of 0.1, train 500 groups of samples with a sample size of $K = 1000$, and randomly select the initial values of the detuning parameters Δ from the range $[-3, 3]$.

Distribution	N	Δ_1	Δ_2	Δ_3	Δ_4	Δ_5	Δ_6	Δ_7	Δ_8	Δ_9
$U(0, 0.2)$	5	-4.8860	0.2452	4.0916	-5.0015	-1.9768				
$U(0, 0.3)$	7	-5.8333	-1.4134	0.4753	-2.6560	9.5803	7.9718	-2.7511		
$U(0, 0.4)$	9	-9.2604	-3.2210	-9.8686	-1.7511	6.9721	7.0765	-1.0804	-0.2291	2.7464

Figure 11(a) shows the relationship between the cost function and the number of iterations for different numbers of detuning parameters in the training process, in order to achieve robust population inversion. During the procedure, the detuning Δ_n is reinitialized if $\Delta_n/\Omega_n > 10$. The reason for doing this is as follows. Physically, the pulse becomes highly detuned and primarily influences the phase rather than the probability amplitude of quantum states when Δ_n is excessively large. As a result, the highly detuned pulse makes little contribution to population transfer, and thus needs to be reinitialized.

An inspection of Fig. 11(a) reveals that the value of the cost function for $N = 9$ is larger than that of other two situations. This is because the sampling ranges of the uniform distribution are different for different pulse numbers. As explained in Sec. III E, a large sampling range leads to a large value of the cost function. Thus, what we care about is not the value of the cost function, but its convergence. When the cost function converges to a small steady value, we can claim that a set of possible solutions for the training parameters is obtained. It is clearly found from Fig. 11(a) that the cost functions do gradually diminish with each subsequent iteration and finally tend to extremely small values, verifying the validity of the gradient descent algorithm and the success of the trainings.

We can also see in Fig. 11(b) that the detuning parameters Δ learned from the training stage perform particularly well in terms of robustness against pulse area errors around $\epsilon_A = 0$. Furthermore, similar to the case of the phase parameters, the system becomes more resilient to the pulse area error when increasing the number of detuning parameters, as illustrated by different robust widths in Fig. 11(b).

B. Supervised learning in high-dimensional spaces

So far, the supervised learning model has mainly been demonstrated to work well in the two-dimensional Hilbert space. Indeed, this model can also be applied in higher-dimensional Hilbert spaces. Next, we take four dimensions as an illustrative example to briefly show how to perform a high-fidelity two-qubit gate in error environments; the treatment in higher dimensions is similar.

Assume that the Hamiltonian of a two-qubit system can be written as

$$H(\Delta^a, \Delta^b) = \Omega(1 + \epsilon_\Omega)\sigma_x^a\sigma_x^b + \Delta^a\sigma_z^a + \Delta^b\sigma_z^b, \quad (30)$$

where Ω is the coupling strength between qubits a and b , Δ^a and Δ^b are the corresponding detunings, and ϵ_Ω denotes a possible error in this system. The objective is to implement a two-qubit gate $U_M = \exp(-i\pi/4\sigma_x^a\sigma_x^b)$, which is actually equivalent to the controlled-NOT (CNOT) gate after performing several single-qubit operations [135].

In the ideal case, i.e., $\epsilon_\Omega = 0$, the target two-qubit gate U_M is readily attained by setting the operation time $T = \pi/(4\Omega)$ and $\Delta^a = \Delta^b = 0$. When taking account of the presence of error ϵ_Ω , we obtain a faulty gate $U_M^f = \exp[-i\pi/4(1 + \epsilon_\Omega)\sigma_x^a\sigma_x^b]$, which is highly sensitive to ϵ_Ω (see the dashed curves in Fig. 12). To improve the robustness with respect to error ϵ_Ω , we adopt a composite pulse sequence and regard the detunings Δ_n^a and Δ_n^b ($n = 1, 2, \dots, N$) as training parameters, i.e., $\Delta = (\Delta_1^a, \Delta_1^b, \dots, \Delta_N^a, \Delta_N^b)$. As shown in Fig. 12, the infidelity is extremely small around $\epsilon_\Omega = 0$ according to the learned detuning parameters, verifying that robust quantum control is also accessible in high-dimensional Hilbert spaces by using this model.

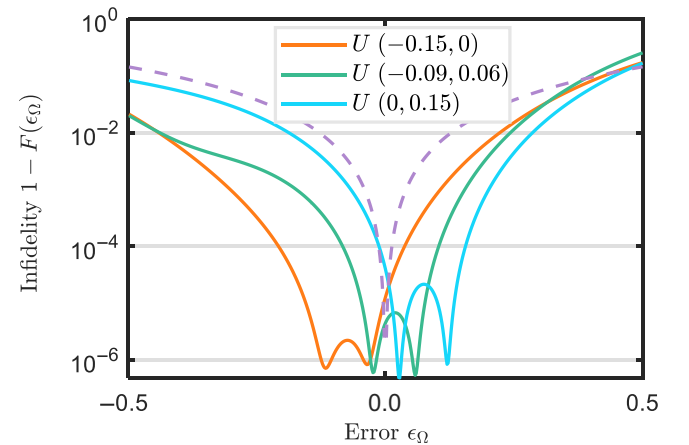


FIG. 12. Infidelity $1 - F(\epsilon_\Omega)$ of the two-qubit gate U_M versus error ϵ_Ω . Each solid profile is plotted according to the learned detuning parameters Δ given in Table III, while the dashed curve is plotted by setting $T = \pi/(4\Omega)$ and $\Delta^a = \Delta^b = 0$.

TABLE III. Learned detuning parameters Δ for implementing the two-qubit gate U_M in a robust manner. We set the duration of each pulse to $T = \pi/(4\Omega)$, adopt a step size of 0.001, choose the pulse number as $N = 9$, train 1000 groups of samples with a sample size of $K = 3000$, and randomly select the initial values of the detuning parameters Δ from the range $[-1, 1]$.

Distribution	Δ_1^a	Δ_2^a	Δ_3^a	Δ_4^a	Δ_5^a	Δ_6^a	Δ_7^a	Δ_8^a	Δ_9^a
$U(-0.15, 0)$	-0.8094	-0.3266	-0.4048	1.0508	1.1646	0.1250	0.1357	-1.5451	0.0231
$U(-0.09, 0.06)$	1.5060	-1.2594	-0.2565	0.6741	-1.6983	1.5649	0.4478	-0.9407	0.5922
$U(0, 0.15)$	-0.3514	1.2741	-0.0107	1.7152	0.2579	-1.9542	-0.4414	-0.9180	0.4095
Distribution	Δ_1^b	Δ_2^b	Δ_3^b	Δ_4^b	Δ_5^b	Δ_6^b	Δ_7^b	Δ_8^b	Δ_9^b
$U(-0.15, 0)$	1.1007	-1.6323	0.5713	1.0148	-1.6145	1.6170	-0.8991	-0.5304	0.8847
$U(-0.09, 0.06)$	-0.2990	-0.9496	-0.6132	0.9016	0.5801	0.5451	0.2672	-0.7618	-0.5137
$U(0, 0.15)$	-1.4707	-0.8018	0.7620	-0.8676	1.6910	0.4098	-0.1400	1.2832	-1.0190

It should be noted that the dimension of the Hilbert space grows exponentially as the number of qubits increases. At this point, successfully training the parameters becomes progressively more difficult for multiple-qubit systems, because the amount of computation will explode. Fortunately, it has been shown that any multi-qubit quantum gate may be constituted from CNOT and single-qubit gates [1], and both types of logic gates can be robustly trained via the current model. Therefore, it is possible to achieve any multiqubit quantum gate in a robust manner using a universal gate set formed by high-fidelity CNOT and single-qubit gates.

VI. CONCLUSION

In conclusion, we have proposed a supervised learning model used for implementing robust quantum control in composite-pulse systems. We first constructed the cost function for this model, and demonstrated how this model works. By introducing two types of virtual variables, we put forward a modified gradient descent algorithm to train phase parameters. We found that the robustness depends heavily on sampling methods. To be specific, the average infidelity tends to enlarge as the sampling range increases, and different sampling distributions result in different robust performances.

Afterwards, we characterized the generalization ability of this model. The results demonstrate that robustness is not greatly improved when the sampling range is too small, whereas robustness is poor once the sampling range exceeds a certain threshold. In particular, there is a corresponding strengthening of the generalization ability when increasing the model complexity (i.e., increasing the pulse number). Therefore, for a given pulse number, a suitable sampling range is conducive to maximizing the generalization ability of the model.

Finally, we demonstrated a wide range of applications for the current model, e.g., robust realization of arbitrary superposition states as well as general single-qubit gates. Specifically, the phase parameters learned from this model perform very well in robustness with respect to various

systematic errors, such as single error, multiple errors, and time-varying errors. It is particularly important that all kinds of situations (including single, multiple, and time-varying errors) can be well tackled in the same model, and the only difference lies in the dimension of the samples. To implement general single-qubit gates in a robust manner, we proposed two different methods, the state-based and evolution operator-based methods, to train the phase parameters with the model's robust property relying on the sampling distribution. Moreover, this model can be applied in higher-dimensional Hilbert spaces, and is suitable for training any physical parameters to attain robust quantum control. It is believed that this supervised learning model provides a universal and high-efficiency plateau for realizing reliable quantum information processing in different quantum systems.

ACKNOWLEDGMENTS

We would like to thank the valuable suggestions of Dr. Ye-Xiong Zeng, Dr. Yanming Che, and Dr. Clemens Gneiting. This work is supported by the Natural Science Foundation of Fujian Province under Grant No. 2021J01575, the Natural Science Funds for Distinguished Young Scholars of Fujian Province under Grant No. 2020J06011, and the Project from Fuzhou University under Grant No. JG202001-2. F.N. is supported in part by Nippon Telegraph and Telephone Corporation (NTT) Research, the Japan Science and Technology Agency (JST) [via the Quantum Leap Flagship Program (Q-LEAP), and the Moonshot R&D Grant No. JPMJMS2061], the Asian Office of Aerospace Research and Development (AOARD) (via Grant No. FA2386-20-1-4069), the Office of Naval Research (ONR Global), and the Foundational Questions Institute Fund (FQXi) via Grant No. FQXi-IAF19-06.

APPENDIX A: SEARCH FOR OPTIMAL SOLUTIONS BY THE ESCAPING METHOD

In this appendix, we mainly demonstrate how to search the optimal solutions by the escaping method, a

synthesis of the modified GRAPE and simulated annealing [124,125]. First, we employ the modified GRAPE algorithm for learning M groups of phase parameters θ_m as a starting point, where $m = 1, \dots, M$. To escape the locally optimal solution, we artificially add a random value to each phase so as to generate new input variables. By making use of the modified GRAPE algorithm again, we obtain the new learned parameters θ'_m and the corresponding average fidelity $\bar{F}'_m(\epsilon_-, \epsilon_+)$, where the subscript m represents the m th group of training sets. If $\bar{F}'_m(\epsilon_-, \epsilon_+) \leq \bar{F}_m(\epsilon_-, \epsilon_+)$ then the new learned parameters θ'_m are not as good as the old ones. However, we accept these new learned parameters θ'_m with probability

$$p_c = \exp \left[- \frac{\bar{F}_m(\epsilon_-, \epsilon_+) - \bar{F}'_m(\epsilon_-, \epsilon_+)}{T_j} \right], \quad (\text{A1})$$

where the sequence $\{T_j\}$ ($j = 1, \dots, J$) is monotonically decreasing, and $T_j > 0$ denotes the temperature in simulated annealing [124,125]. On the other hand, if $\bar{F}'_m(\epsilon_-, \epsilon_+) > \bar{F}_m(\epsilon_-, \epsilon_+)$, it indicates that the solution has jumped out of locally optimal regions, and thus we accept the new ones. After updating each training group J times, we next calculate the total average fidelity for all training groups,

$$\bar{F}_{\text{tot}} = \frac{1}{M} \sum_{m=1}^M \bar{F}_m(\epsilon_-, \epsilon_+). \quad (\text{A2})$$

Then, the learned parameters whose average fidelities are lower than \bar{F}_{tot} are discarded. This iteration process continues until the threshold of the total average fidelity is reached; see Algorithm 2 for details. At the end, the optimal solutions for robust quantum control are left.

ALGORITHM 2. Escape-based GRAPE algorithm.

1. Use the modified GRAPE algorithm to learn M group parameters θ_m and calculate the average fidelity $\bar{F}_m(\epsilon_-, \epsilon_+)$.
 2. Add random values $\delta\theta_n^m$ to the phase parameters: $\theta_n^m \leftarrow \theta_n^m + \delta\theta_n^m$, the new input variables.
 3. Reuse the modified GRAPE algorithm to learn new parameters θ'_m and the average fidelity $\bar{F}'_m(\epsilon_-, \epsilon_+)$.
 4. If $\bar{F}'_m(\epsilon_-, \epsilon_+) < \bar{F}_m(\epsilon_-, \epsilon_+)$ then $\theta_m \leftarrow \theta'_m$ and $\bar{F}_m(\epsilon_-, \epsilon_+) \leftarrow \bar{F}'_m(\epsilon_-, \epsilon_+)$. Otherwise, accept θ'_m with probability p_c in Eq. (A1).
 5. Repeat steps 2 through 4 J times.
 6. Calculate the total average fidelity \bar{F}_{tot} .
 7. Discard learned parameters θ_m when $\bar{F}_m(\epsilon_-, \epsilon_+) < \bar{F}_{\text{tot}}$.
 8. Go to step 2 until $(\max\{\bar{F}_m(\epsilon_-, \epsilon_+)\} - \bar{F}_{\text{tot}}) < \epsilon$.
-

APPENDIX B: COMMON SAMPLING DISTRIBUTIONS

This appendix briefly introduces several common sampling distributions.

(i) *Uniform distribution* $U(\epsilon_-, \epsilon_+)$. The probability density function of the uniform distribution reads

$$\rho_u(\epsilon) = \begin{cases} \frac{1}{\epsilon_+ - \epsilon_-}, & \epsilon \in [\epsilon_-, \epsilon_+], \\ 0, & \text{otherwise,} \end{cases} \quad (\text{B1})$$

with sampling interval $[\epsilon_-, \epsilon_+]$. The expectation and variance are

$$\mathcal{E}(\epsilon) = \frac{\epsilon_+ + \epsilon_-}{2}, \quad \mathcal{D}(\epsilon) = \frac{(\epsilon_+ - \epsilon_-)^2}{12}. \quad (\text{B2})$$

(ii) *Gaussian distribution* $G(\mu, \nu)$. The probability density function of the Gaussian distribution reads

$$\rho_g(\epsilon) = \frac{1}{\sqrt{2\pi\nu}} \exp \left[- \frac{(\epsilon - \mu)^2}{2\nu^2} \right]. \quad (\text{B3})$$

The expectation and variance are

$$\mathcal{E}(\epsilon) = \mu, \quad \mathcal{D}(\epsilon) = \nu^2. \quad (\text{B4})$$

(iii) *Exponential distribution* $E(\lambda)$. The probability density function of the exponential distribution reads

$$\rho_e(\epsilon) = \begin{cases} \frac{1}{\lambda} \exp \left(- \frac{\epsilon}{\lambda} \right), & \epsilon \geq 0, \\ 0, & \epsilon < 0, \end{cases} \quad (\text{B5})$$

with rate parameter λ . The expectation and variance are

$$\mathcal{E}(\epsilon) = \lambda, \quad \mathcal{D}(\epsilon) = \lambda^2. \quad (\text{B6})$$

(iv) *Beta distribution* $B(\alpha, \beta)$. The probability density function of the beta distribution reads

$$\rho_b(\epsilon) = \frac{\Gamma(\alpha + \beta)}{\Gamma(\alpha)\Gamma(\beta)} \epsilon^{\alpha-1} (1 - \epsilon)^{\beta-1}, \quad (\text{B7})$$

where $\Gamma(\cdot)$ is the gamma function. The expectation and variance are

$$\mathcal{E}(\epsilon) = \frac{\alpha}{\alpha + \beta}, \quad \mathcal{D}(\epsilon) = \frac{\alpha\beta}{(\alpha + \beta)^2(\alpha + \beta + 1)}. \quad (\text{B8})$$

[1] M. A. Nielsen and I. L. Chuang, *Quantum Computation and Quantum Information* (Cambridge University Press, Cambridge, 2000).

- [2] L. Allen and J. H. Eberly, *Optical Resonance and Two-Level Atoms* (Dover Publications, New York, 1975).
- [3] N. V. Vitanov, T. Halfmann, B. W. Shore, and K. Bergmann, Laser-induced population transfer by adiabatic passage techniques, *Annu. Rev. Phys. Chem.* **52**, 763 (2001).
- [4] Y.-X. Liu, J. Q. You, L. F. Wei, C. P. Sun, and F. Nori, Optical selection rules and phase-dependent adiabatic state control in a superconducting quantum circuit, *Phys. Rev. Lett.* **95**, 087001 (2005).
- [5] P. Král, I. Thanopoulos, and M. Shapiro, Colloquium: Coherently controlled adiabatic passage, *Rev. Mod. Phys.* **79**, 53 (2007).
- [6] N. V. Vitanov, A. A. Rangelov, B. W. Shore, and K. Bergmann, Stimulated Raman adiabatic passage in physics, chemistry, and beyond, *Rev. Mod. Phys.* **89**, 015006 (2017).
- [7] L. Viola, E. Knill, and S. Lloyd, Dynamical decoupling of open quantum systems, *Phys. Rev. Lett.* **82**, 2417 (1999).
- [8] K. Khodjasteh and D. A. Lidar, Fault-tolerant quantum dynamical decoupling, *Phys. Rev. Lett.* **95**, 180501 (2005).
- [9] A. M. Souza, G. A. Álvarez, and D. Suter, Robust dynamical decoupling, *Phil. Trans. R. Soc. A* **370**, 4748 (2012).
- [10] S. Ashhab and F. Nori, Control-free control: Manipulating a quantum system using only a limited set of measurements, *Phys. Rev. A* **82**, 062103 (2010).
- [11] H. M. Wiseman, Squinting at quantum systems, *Nature* **470**, 178 (2011).
- [12] N. Yang, J. Zhang, H. Wang, Y.-X. Liu, R.-B. Wu, L.-Q. Liu, C.-W. Li, and F. Nori, Noise suppression of on-chip mechanical resonators by chaotic coherent feedback, *Phys. Rev. A* **92**, 033812 (2015).
- [13] J. Zhang, Y.-X. Liu, R.-B. Wu, K. Jacobs, and F. Nori, Quantum feedback: Theory, experiments, and applications, *Phys. Rep.* **679**, 1 (2017).
- [14] D. Daems, A. Ruschhaupt, D. Sugny, and S. Guérin, Robust quantum control by a single-shot shaped pulse, *Phys. Rev. Lett.* **111**, 050404 (2013).
- [15] L. Van-Damme, D. Schraft, G. T. Genov, D. Sugny, T. Halfmann, and S. Guérin, Robust NOT gate by single-shot-shaped pulses: Demonstration of the efficiency of the pulses in rephasing atomic coherences, *Phys. Rev. A* **96**, 022309 (2017).
- [16] F. Motzoi, J. M. Gambetta, P. Rebentrost, and F. K. Wilhelm, Simple pulses for elimination of leakage in weakly nonlinear qubits, *Phys. Rev. Lett.* **103**, 110501 (2009).
- [17] R. Schutjens, F. A. Dagga, D. J. Egger, and F. K. Wilhelm, Single-qubit gates in frequency-crowded transmon systems, *Phys. Rev. A* **88**, 052330 (2013).
- [18] L. S. Theis, F. Motzoi, F. K. Wilhelm, and M. Saffman, High-fidelity Rydberg-blockade entangling gate using shaped, analytic pulses, *Phys. Rev. A* **94**, 032306 (2016).
- [19] C. Chen, D. Dong, R. Long, I. R. Petersen, and H. A. Rabitz, Sampling-based learning control of inhomogeneous quantum ensembles, *Phys. Rev. A* **89**, 023402 (2014).
- [20] D. Dong, M. A. Mabrok, I. R. Petersen, B. Qi, C. Chen, and H. Rabitz, Sampling-based learning control for quantum systems with uncertainties, *IEEE Trans. Control Syst. Technol.* **23**, 2155 (2015).
- [21] D. Dong, X. Xing, H. Ma, C. Chen, Z. Liu, and H. Rabitz, Learning-based quantum robust control: Algorithm, applications, and experiments, *IEEE Trans. Cybern.* **50**, 3581 (2020).
- [22] L. Van Damme, Q. Ansel, S. J. Glaser, and D. Sugny, Robust optimal control of two-level quantum systems, *Phys. Rev. A* **95**, 063403 (2017).
- [23] G. Dridi, K. Liu, and S. Guérin, Optimal robust quantum control by inverse geometric optimization, *Phys. Rev. Lett.* **125**, 250403 (2020).
- [24] L.-N. Sun, L.-L. Yan, S.-L. Su, and Y. Jia, One-step implementation of time-optimal-control three-qubit nonadiabatic holonomic controlled gates in Rydberg atoms, *Phys. Rev. Appl.* **16**, 064040 (2021).
- [25] D. Yu, H. Wang, J.-M. Liu, S.-L. Su, J. Qian, and W. Zhang, Multiqubit Toffoli gates and optimal geometry with Rydberg atoms, *Phys. Rev. Appl.* **18**, 034072 (2022).
- [26] J.-F. Wei, F.-Q. Guo, D.-Y. Wang, Y. Jia, L.-L. Yan, M. Feng, and S.-L. Su, Fast multiqubit Rydberg geometric fan-out gates with optimal control technology, *Phys. Rev. A* **105**, 042404 (2022).
- [27] H. Zhang and H. Rabitz, Robust optimal control of quantum molecular systems in the presence of disturbances and uncertainties, *Phys. Rev. A* **49**, 2241 (1994).
- [28] L. Van Damme, D. Sugny, and S. J. Glaser, Application of the small-tip-angle approximation in the toggling frame for the design of analytic robust pulses in quantum control, *Phys. Rev. A* **104**, 042226 (2021).
- [29] X. Laforgue, G. Dridi, and S. Guérin, Optimal quantum control robust against pulse inhomogeneities: Analytic solutions, *Phys. Rev. A* **106**, 052608 (2022).
- [30] T. Propson, B. E. Jackson, J. Koch, Z. Manchester, and D. I. Schuster, Robust quantum optimal control with trajectory optimization, *Phys. Rev. Appl.* **17**, 014036 (2022).
- [31] M. Mohan, R. de Keijzer, and S. Kokkelmans, Robust control and optimal Rydberg states for neutral atom two-qubit gates, *Phys. Rev. Res.* **5**, 033052 (2023).
- [32] M. Mohri, A. Rostamizadeh, and A. Talwalkar, *Foundations of Machine Learning* (MIT Press, Cambridge, 2012).
- [33] G. Bonaccorso, *Machine Learning Algorithms* (Packt Publishing, Birmingham, 2017).
- [34] J. Biamonte, P. Wittek, N. Pancotti, P. Rebentrost, N. Wiebe, and S. Lloyd, Quantum machine learning, *Nature* **549**, 195 (2017).
- [35] V. Dunjko and H. J. Briegel, Machine learning & artificial intelligence in the quantum domain: A review of recent progress, *Rep. Prog. Phys.* **81**, 074001 (2018).
- [36] G. Carleo, I. Cirac, K. Cranmer, L. Daudet, M. Schuld, N. Tishby, L. Vogt-Maranto, and L. Zdeborová, Machine learning and the physical sciences, *Rev. Mod. Phys.* **91**, 045002 (2019).
- [37] L. Arrachea, Energy dynamics, heat production and heat-work conversion with qubits: Toward the development of quantum machines, *Rep. Prog. Phys.* **86**, 036501 (2023).
- [38] M. Krenn, J. Landgraf, T. Foesel, and F. Marquardt, Artificial intelligence and machine learning for quantum technologies, *Phys. Rev. A* **107**, 010101 (2023).

- [39] C. Zhang and X. Wang, Spin-qubit noise spectroscopy from randomized benchmarking by supervised learning, *Phys. Rev. A* **99**, 042316 (2019).
- [40] Y. Zeng, J. Shen, S. Hou, T. Gebremariam, and C. Li, Quantum control based on machine learning in an open quantum system, *Phys. Lett. A* **384**, 126886 (2020).
- [41] Y. Che, C. Gneiting, T. Liu, and F. Nori, Topological quantum phase transitions retrieved through unsupervised machine learning, *Phys. Rev. B* **102**, 1342130 (2020).
- [42] Y. Ding, Y. Ban, J. D. Martín-Guerrero, E. Solano, J. Casanova, and X. Chen, Breaking adiabatic quantum control with deep learning, *Phys. Rev. A* **103**, L040401 (2021).
- [43] M.-Z. Ai, Y. Ding, Y. Ban, J. D. Martín-Guerrero, J. Casanova, J.-M. Cui, Y.-F. Huang, X. Chen, C.-F. Li, and G.-C. Guo, Experimentally realizing efficient quantum control with reinforcement learning, *Sci. China Phys. Mech. Astron.* **65**, 250312 (2022).
- [44] S. Ahmed, C. Sánchez Muñoz, F. Nori, and A. F. Kockum, Quantum state tomography with conditional generative adversarial networks, *Phys. Rev. Lett.* **127**, 140502 (2021).
- [45] T. Huang, Y. Ban, E. Y. Sherman, and X. Chen, Machine-learning-assisted quantum control in a random environment, *Phys. Rev. Appl.* **17**, 024040 (2022).
- [46] R.-B. Wu, X. Cao, P. Xie, and Y.-X. Liu, End-to-end quantum machine learning implemented with controlled quantum dynamics, *Phys. Rev. Appl.* **14**, 064020 (2020).
- [47] D. F. Wise, J. J. Morton, and S. Dhomkar, Using deep learning to understand and mitigate the qubit noise environment, *PRX Quantum* **2**, 010316 (2021).
- [48] Y.-C. Ma and M.-H. Yung, Transforming Bell's inequalities into state classifiers with machine learning, *npj Quantum Inf.* **4**, 34 (2018).
- [49] I. Glasser, N. Pancotti, M. August, I. D. Rodriguez, and J. I. Cirac, Neural-network quantum states, string-bond states, and chiral topological states, *Phys. Rev. X* **8**, 011006 (2018).
- [50] J. Gao, L.-F. Qiao, Z.-Q. Jiao, Y.-C. Ma, C.-Q. Hu, R.-J. Ren, A.-L. Yang, H. Tang, M.-H. Yung, and X.-M. Jin, Experimental machine learning of quantum states, *Phys. Rev. Lett.* **120**, 240501 (2018).
- [51] C. Harney, S. Pirandola, A. Ferraro, and M. Paternostro, Entanglement classification via neural network quantum states, *New J. Phys.* **22**, 045001 (2020).
- [52] S. Ahmed, C. Sánchez Muñoz, F. Nori, and A. F. Kockum, Classification and reconstruction of optical quantum states with deep neural networks, *Phys. Rev. Res.* **3**, 033278 (2021).
- [53] S. V. Vintskevich, N. Bao, A. Nomerotski, P. Stankus, and D. A. Grigoriev, Classification of four-qubit entangled states via machine learning, *Phys. Rev. A* **107**, 032421 (2023).
- [54] E. Zahedinejad, J. Ghosh, and B. C. Sanders, Designing high-fidelity single-shot three-qubit gates: A machine-learning approach, *Phys. Rev. Appl.* **6**, 054005 (2016).
- [55] X.-C. Yang, M.-H. Yung, and X. Wang, Neural-network-designed pulse sequences for robust control of singlet-triplet qubits, *Phys. Rev. A* **97**, 042324 (2018).
- [56] K. K. Sabapathy, H. Qi, J. Izaac, and C. Weedbrook, Production of photonic universal quantum gates enhanced by machine learning, *Phys. Rev. A* **100**, 012326 (2019).
- [57] R. J. Spiteri, M. Schmidt, J. Ghosh, E. Zahedinejad, and B. C. Sanders, Quantum control for high-fidelity multi-qubit gates, *New J. Phys.* **20**, 113009 (2018).
- [58] J. M. Arrazola, T. R. Bromley, J. Izaac, C. R. Myers, K. Brádler, and N. Killoran, Machine learning method for state preparation and gate synthesis on photonic quantum computers, *Quantum Sci. Technol.* **4**, 024004 (2019).
- [59] R. S. Gupta and M. J. Biercuk, Machine learning for predictive estimation of qubit dynamics subject to dephasing, *Phys. Rev. Appl.* **9**, 064042 (2018).
- [60] Y. Baum, M. Amico, S. Howell, M. Hush, M. Liuzzi, P. Mundada, T. Merkh, A. R. Carvalho, and M. J. Biercuk, Experimental deep reinforcement learning for error-robust gate-set design on a superconducting quantum computer, *PRX Quantum* **2**, 040324 (2021).
- [61] Y. Zeng, Z.-Y. Zhou, E. Rinaldi, C. Gneiting, and F. Nori, Approximate autonomous quantum error correction with reinforcement learning, *Phys. Rev. Lett.* **131**, 050601 (2023).
- [62] R. Porotti, V. Peano, and F. Marquardt, Gradient-ascent pulse engineering with feedback, *PRX Quantum* **4**, 030305 (2023).
- [63] V. F. Krotov, *Global Methods in Optimal Control Theory* (Dekker, New York, 1996).
- [64] N. Khaneja, T. Reiss, C. Kehlet, T. Schulte-Herbrüggen, and S. J. Glaser, Optimal control of coupled spin dynamics: Design of NMR pulse sequences by gradient ascent algorithms, *J. Magn. Reson.* **172**, 296 (2005).
- [65] N. B. Lovett, C. Crosnier, M. Perarnau-Llobet, and B. C. Sanders, Differential evolution for many-particle adaptive quantum metrology, *Phys. Rev. Lett.* **110**, 220501 (2013).
- [66] E. Zahedinejad, J. Ghosh, and B. C. Sanders, High-fidelity single-shot Toffoli gate via quantum control, *Phys. Rev. Lett.* **114**, 200502 (2015).
- [67] Y. Huang, Q. Li, X. Hou, R.-B. Wu, M.-H. Yung, A. Bayat, and X. Wang, Robust resource-efficient quantum variational ansatz through an evolutionary algorithm, *Phys. Rev. A* **105**, 052414 (2022).
- [68] A. B. Magann, C. Arenz, M. D. Grace, T.-S. Ho, R. L. Kosut, J. R. McClean, H. A. Rabitz, and M. Sarovar, From pulses to circuits and back again: A quantum optimal control perspective on variational quantum algorithms, *PRX Quantum* **2**, 010101 (2021).
- [69] J. Roslund and H. Rabitz, Gradient algorithm applied to laboratory quantum control, *Phys. Rev. A* **79**, 053417 (2009).
- [70] J. Johansson, P. Nation, and F. Nori, QuTiP 2: A Python framework for the dynamics of open quantum systems, *Comp. Phys. Comm.* **184**, 1234 (2013).
- [71] R.-B. Wu, H. Ding, D. Dong, and X. Wang, Learning robust and high-precision quantum controls, *Phys. Rev. A* **99**, 042327 (2019).
- [72] X. Ge, H. Ding, H. Rabitz, and R.-B. Wu, Robust quantum control in games: An adversarial learning approach, *Phys. Rev. A* **101**, 052317 (2020).
- [73] H.-J. Ding, B. Chu, B. Qi, and R.-B. Wu, Collaborative learning of high-precision quantum control and tomography, *Phys. Rev. Appl.* **16**, 014056 (2021).

- [74] B. Li, S. Ahmed, S. Saraogi, N. Lambert, F. Nori, A. Pitchford, and N. Shammah, Pulse-level noisy quantum circuits with QuTiP, *Quantum* **6**, 630 (2022).
- [75] P. Doria, T. Calarco, and S. Montangero, Optimal control technique for many-body quantum dynamics, *Phys. Rev. Lett.* **106**, 190501 (2011).
- [76] T. Caneva, T. Calarco, and S. Montangero, Chopped random-basis quantum optimization, *Phys. Rev. A* **84**, 022326 (2011).
- [77] N. Rach, M. M. Müller, T. Calarco, and S. Montangero, Dressing the chopped-random-basis optimization: A bandwidth-limited access to the trap-free landscape, *Phys. Rev. A* **92**, 062343 (2015).
- [78] J. J. W. H. Sørensen, M. O. Aramburu, T. Heinzl, and J. F. Sherson, Quantum optimal control in a chopped basis: Applications in control of Bose-Einstein condensates, *Phys. Rev. A* **98**, 022119 (2018).
- [79] P. de Fouquieres, S. Schirmer, S. Glaser, and I. Kuprov, Second order gradient ascent pulse engineering, *J. Magn. Reson.* **212**, 412 (2011).
- [80] J. Nocedal and S. J. Wright, *Numerical Optimization* (Springer, Berlin, 2006).
- [81] B. T. Torosov, B. W. Shore, and N. V. Vitanov, Coherent control techniques for two-state quantum systems: A comparative study, *Phys. Rev. A* **103**, 033110 (2021).
- [82] X. Wang, L. S. Bishop, J. Kestner, E. Barnes, K. Sun, and S. Das Sarma, Composite pulses for robust universal control of singlet-triplet qubits, *Nat. Commun.* **3**, 997 (2012).
- [83] X. Wang, L. S. Bishop, E. Barnes, J. P. Kestner, and S. Das Sarma, Robust quantum gates for singlet-triplet spin qubits using composite pulses, *Phys. Rev. A* **89**, 022310 (2014).
- [84] M. O. Scully and M. S. Zubairy, *Quantum Optics* (Cambridge University Press, Cambridge, UK, 1997).
- [85] G. T. Genov, D. Schraft, N. V. Vitanov, and T. Halfmann, Arbitrarily accurate pulse sequences for robust dynamical decoupling, *Phys. Rev. Lett.* **118**, 133202 (2017).
- [86] G. T. Genov, M. Hain, N. V. Vitanov, and T. Halfmann, Universal composite pulses for efficient population inversion with an arbitrary excitation profile, *Phys. Rev. A* **101**, 013827 (2020).
- [87] E. Kyoseva, H. Greener, and H. Suchowski, Detuning-modulated composite pulses for high-fidelity robust quantum control, *Phys. Rev. A* **100**, 032333 (2019).
- [88] I. Kaplan, M. Erew, Y. Piasetzky, M. Goldstein, Y. Oz, and H. Suchowski, Segmented composite design of robust single-qubit quantum gates, *Phys. Rev. A* **108**, 042401 (2023).
- [89] M. H. Levitt and R. Freeman, NMR population inversion using a composite pulse, *J. Magn. Reson.* **33**, 473 (1979).
- [90] M. H. Levitt, Composite pulses, *Prog. NMR Spectrosc.* **18**, 61 (1986).
- [91] S. Wimperis, Broadband, narrowband, and passband composite pulses for use in advanced NMR experiments, *J. Magn. Reson.* **109**, 221 (1994).
- [92] H. K. Cummins, G. Llewellyn, and J. A. Jones, Tackling systematic errors in quantum logic gates with composite rotations, *Phys. Rev. A* **67**, 042308 (2003).
- [93] K. R. Brown, A. W. Harrow, and I. L. Chuang, Arbitrarily accurate composite pulse sequences, *Phys. Rev. A* **70**, 052318 (2004).
- [94] T. Ichikawa, M. Bando, Y. Kondo, and M. Nakahara, Designing robust unitary gates: Application to concatenated composite pulses, *Phys. Rev. A* **84**, 062311 (2011).
- [95] J. A. Jones, Designing short robust NOT gates for quantum computation, *Phys. Rev. A* **87**, 052317 (2013).
- [96] I. Cohen, A. Rotem, and A. Retzker, Refocusing two-qubit-gate noise for trapped ions by composite pulses, *Phys. Rev. A* **93**, 032340 (2016).
- [97] G. Dridi, M. Mejatty, S. J. Glaser, and D. Sugny, Robust control of a NOT gate by composite pulses, *Phys. Rev. A* **101**, 012321 (2020).
- [98] B. T. Torosov and N. V. Vitanov, High-fidelity composite quantum gates for Raman qubits, *Phys. Rev. Res.* **2**, 043194 (2020).
- [99] J. F. F. Bulmer, J. A. Jones, and I. A. Walmsley, Drive-noise tolerant optical switching inspired by composite pulses, *Opt. Express* **28**, 8646 (2020).
- [100] X. Rong, J. Geng, F. Shi, Y. Liu, K. Xu, W. Ma, F. Kong, Z. Jiang, Y. Wu, and J. F. Du, Experimental fault-tolerant universal quantum gates with solid-state spins under ambient conditions, *Nat. Commun.* **6**, 8748 (2015).
- [101] E. Mount, C. Kabytayev, S. Crain, R. Harper, S.-Y. Baek, G. Vrijsen, S. T. Flammia, K. R. Brown, P. Maunz, and J. Kim, Error compensation of single-qubit gates in a surface-electrode ion trap using composite pulses, *Phys. Rev. A* **92**, 060301 (2015).
- [102] S. S. Ivanov, B. T. Torosov, and N. V. Vitanov, High-fidelity quantum control by polychromatic pulse trains, *Phys. Rev. Lett.* **129**, 240505 (2022).
- [103] B. T. Torosov and N. V. Vitanov, Experimental demonstration of composite pulses on IBM's quantum computer, *Phys. Rev. Appl.* **18**, 034062 (2022).
- [104] B. T. Torosov and N. V. Vitanov, Smooth composite pulses for high-fidelity quantum information processing, *Phys. Rev. A* **83**, 053420 (2011).
- [105] G. T. Genov, D. Schraft, T. Halfmann, and N. V. Vitanov, Correction of arbitrary field errors in population inversion of quantum systems by universal composite pulses, *Phys. Rev. Lett.* **113**, 043001 (2014).
- [106] G. H. Low, T. J. Yoder, and I. L. Chuang, Optimal arbitrarily accurate composite pulse sequences, *Phys. Rev. A* **89**, 022341 (2014).
- [107] B. T. Torosov and N. V. Vitanov, Arbitrarily accurate twin composite π -pulse sequences, *Phys. Rev. A* **97**, 043408 (2018).
- [108] G. Demeter, Composite pulses for high-fidelity population inversion in optically dense, inhomogeneously broadened atomic ensembles, *Phys. Rev. A* **93**, 023830 (2016).
- [109] Z.-C. Shi, H.-N. Wu, L.-T. Shen, J. Song, Y. Xia, X. X. Yi, and S.-B. Zheng, Robust single-qubit gates by composite pulses in three-level systems, *Phys. Rev. A* **103**, 052612 (2021).
- [110] H. L. Gevorgyan and N. V. Vitanov, Ultrahigh-fidelity composite rotational quantum gates, *Phys. Rev. A* **104**, 012609 (2021).

- [111] B. T. Torosov, M. Drewsen, and N. V. Vitanov, Chiral resolution by composite Raman pulses, *Phys. Rev. Res.* **2**, 043235 (2020).
- [112] Z.-C. Shi, C. Zhang, D. Ran, Y. Xia, R. Ianculescu, A. Friedman, X. X. Yi, and S.-B. Zheng, Composite pulses for high fidelity population transfer in three-level systems, *New J. Phys.* **24**, 023014 (2022).
- [113] H.-N. Wu, C. Zhang, J. Song, Y. Xia, and Z.-C. Shi, Composite pulses for optimal robust control in two-level systems, *Phys. Rev. A* **107**, 023103 (2023).
- [114] A. D'Arrigo, G. Falci, and E. Paladino, High-fidelity two-qubit gates via dynamical decoupling of local $1/f$ noise at the optimal point, *Phys. Rev. A* **94**, 022303 (2016).
- [115] C.-H. Huang and H.-S. Goan, Robust quantum gates for stochastic time-varying noise, *Phys. Rev. A* **95**, 062325 (2017).
- [116] J. P. Kestner, X. Wang, L. S. Bishop, E. Barnes, and S. Das Sarma, Noise-resistant control for a spin qubit array, *Phys. Rev. Lett.* **110**, 140502 (2013).
- [117] X. Wang, F. A. Calderon-Vargas, M. S. Rana, J. P. Kestner, E. Barnes, and S. Das Sarma, Noise-compensating pulses for electrostatically controlled silicon spin qubits, *Phys. Rev. B* **90**, 155306 (2014).
- [118] R. K. L. Colmenar and J. P. Kestner, Reverse engineering of one-qubit filter functions with dynamical invariants, *Phys. Rev. A* **106**, 032611 (2022).
- [119] A. R. Milne, C. L. Edmunds, C. Hempel, F. Roy, S. Mavadia, and M. J. Biercuk, Phase-modulated entangling gates robust to static and time-varying errors, *Phys. Rev. Appl.* **13**, 024022 (2020).
- [120] M. Kang, Y. Wang, C. Fang, B. Zhang, O. Khosravani, J. Kim, and K. R. Brown, Designing filter functions of frequency-modulated pulses for high-fidelity two-qubit gates in ion chains, *Phys. Rev. Appl.* **19**, 014014 (2023).
- [121] T. Araki, F. Nori, and C. Gneiting, Robust quantum control with disorder-dressed evolution, *Phys. Rev. A* **107**, 032609 (2023).
- [122] I. Khalid, C. A. Weidner, E. A. Jonckheere, S. G. Shermer, and F. C. Langbein, Statistically characterizing robustness and fidelity of quantum controls and quantum control algorithms, *Phys. Rev. A* **107**, 032606 (2023).
- [123] G. Bhole, Ph.D. thesis, University of Oxford, 2020.
- [124] M. H. Ram, V. R. Krithika, P. Batra, and T. S. Mahesh, Robust quantum control using hybrid pulse engineering, *Phys. Rev. A* **105**, 042437 (2022).
- [125] T. S. Mahesh, P. Batra, and M. H. Ram, Quantum optimal control: Practical aspects and diverse methods, *J. Indian Inst. Sci.* **103**, 591 (2023).
- [126] C. M. Bishop, *Pattern Recognition and Machine Learning* (Springer, Singapore, 2006).
- [127] R. Freeman, *Spin Choreography* (Spektrum, Oxford, 1997).
- [128] T. J. Green, J. Sastrawan, H. Uys, and M. J. Biercuk, Arbitrary quantum control of qubits in the presence of universal noise, *New J. Phys.* **15**, 095004 (2013).
- [129] C. Kabytayev, T. J. Green, K. Khodjasteh, M. J. Biercuk, L. Viola, and K. R. Brown, Robustness of composite pulses to time-dependent control noise, *Phys. Rev. A* **90**, 012316 (2014).
- [130] G. A. Paz-Silva and L. Viola, General transfer-function approach to noise filtering in open-loop quantum control, *Phys. Rev. Lett.* **113**, 250501 (2014).
- [131] X.-L. Zhen, T. Xin, F.-H. Zhang, and G.-L. Long, Experimental demonstration of concatenated composite pulses robustness to non-static errors, *Sci. China Phys. Mech. Astron.* **59**, 103011 (2016).
- [132] H. Haas, D. Puzzuoli, F. Zhang, and D. G. Cory, Engineering effective Hamiltonians, *New J. Phys.* **21**, 103011 (2019).
- [133] B. Li, F. A. Calderon-Vargas, J. Zeng, and E. Barnes, Designing arbitrary single-axis rotations robust against perpendicular time-dependent noise, *New J. Phys.* **23**, 093032 (2021).
- [134] Q. D. Su, R. Bruinsma, and W. C. Campbell, Quantum gates robust to secular amplitude drifts, *Phys. Rev. A* **104**, 052625 (2021).
- [135] T. Gefen, D. Cohen, I. Cohen, and A. Retzker, Enhancing the fidelity of two-qubit gates by measurements, *Phys. Rev. A* **95**, 032314 (2017).